

Dissertation  
submitted to the  
Combined Faculties for the Natural Sciences and for Mathematics  
of the Ruperto-Carola-University of Heidelberg, Germany  
for the degree of  
Doctor of Natural Sciences

Put forward by  
Oleksiy Golubov  
born in: Zaporizhya, Ukraine  
Oral examination: 9<sup>th</sup> November, 2012



# Modelling the Milky Way Disc

Referee: apl. Prof. Dr. Andreas Just  
Prof. Dr. Hans-Walter Rix



## Abstract

RAVE, SEGUE and Hipparcos data are used to study the dynamics of stars in the extended solar neighbourhood. The asymmetric drift of thin disc dwarfs is studied as a function of colour and metallicity. Linear extrapolation of the data falls within the error bars from Aumer & Binney (2009) for local standard of rest. The observed metallicity dependence of the asymmetric drift is consistent with the known radial metallicity distribution in the disc. Implying the asymmetric drift correction to the SEGUE data allows us to reconstruct the behaviour of the rotation curve of the Milky Way in the extended solar neighbourhood. The rotation curve appears to be essentially flat, giving no hint for a dip just outside the solar radius followed by an increase observed in some other data sets. The data are supplemented by tangent point measurements for the inner rotation curve. Thus a synthetic rotation curve of the Milky Way is obtained. It is fitted by a density model consisting of a Dehnen bulge, an exponential disc with a hole, and a flattened dark matter halo with either cored isothermal or NFW density profile. In this fitting the parameters are constrained to reproduce the local surface density of the disc and the local volume density of the halo, which are known from local stellar dynamics in the solar neighbourhood. Thus the density model of the Milky Way is reconstructed. The vertical structure of the disc of the Milky Way is consistent with the model by Just & Jahreiß (2010). Some basic features of distribution functions of the Milky Way and of the dynamical heating are also discussed.

## Inhaltsangabe

RAVE, SEGUE und Hipparcos Daten wurden verwendet, um Sterndynamik in der erweiterten Solarnachbarschaft zu studieren. Die asymmetrische Drift von den Zwergen von der Dünnscheibe Zwergen ist als eine Funktion der Farbe und Metallizität untersucht worden. Lineare Extrapolation der Daten stimmt mit dem lokalen Standard der Ruhe von Aumer & Binney (2009) überein. Die beobachtete Abhängigkeit der asymmetrischen Drift von der Metallizität ist konsistent mit der bekannten radialen Verteilung in Metallizität von der Scheibe. Die Korrektur von den SEGUE Daten für die asymmetrische Drift erlaubt die Rotationskurve der Milchstraße in dem erweiterten Solarnachbarschaft zu rekonstruieren. Die Rotationskurve ist eigentlich flach, mit keinem Sprung außerhalb des Sonnensystems Radius und keinem Anstieg danach, die in manche anderen Datensätzen beobachtet wurden. Die Daten werden durch Tangentenpunktmeßungen von der Innenrotationkurve ergänzt. Daß erlaubt eine synthetische Rotationskurve der Milchstraße zu rekonstruieren. Die wird mit einem Dichtemodell angepaßt, dieses besteht aus Dehnen Bulge, eine exponentielle Scheibe mit einem Loch und einem abgeflachten Halo aus Dunklematerie mit entweder entkernt isothermen oder NFW Dichteprofil. In dieser Anpaßung sind die Parameter gezwungen, die lokalen Flächendichte der Scheibe und der örtlichen Volumensdichte des Halos zu reproduzieren, die von lokalen Sterndynamik im Sonnensystemnachbarschaft bekannt sind. Damit ist die Dichtemodell der Milchstraße rekonstruiert. Die vertikale Struktur der Scheibe der Milchstraße steht im Einklang mit dem Modell von Just & Jahreiß (2010). Einige grundlegende Merkmale von Verteilungsfunktionen der Milchstraße und des dynamischen Heizung werden auch diskutiert.



# Contents

<b>1</b>	<b>Introduction</b>	<b>1</b>
1.1	What it is all about . . . . .	1
1.1.1	What is the Galaxy? . . . . .	1
1.1.2	What the Galaxy is not? . . . . .	1
1.1.3	Why study the Galaxy? . . . . .	2
1.1.4	How study the Galaxy? . . . . .	2
1.2	Formation of the Galaxy . . . . .	3
1.3	Structure of the Galaxy . . . . .	4
1.3.1	The halo . . . . .	4
1.3.2	The bulge . . . . .	4
1.3.3	The disc . . . . .	5
1.4	Stellar dynamics . . . . .	5
1.5	Surveys of the Galaxy . . . . .	6
1.6	State of the art . . . . .	8
<b>2</b>	<b>Data analysis</b>	<b>9</b>
2.1	Used data sets . . . . .	9
2.1.1	RAVE . . . . .	9
2.1.2	Hipparcos . . . . .	9
2.1.3	SEGUE G-dwarfs . . . . .	9
2.1.4	SEGUE M-dwarfs . . . . .	11
2.2	Rotation curve data . . . . .	15
2.2.1	Observations of the rotation curve . . . . .	15
2.2.2	Rescaling the data . . . . .	15
<b>3</b>	<b>Vertical structure of the disc</b>	<b>17</b>
3.1	A self-consistent local disk model . . . . .	17
3.2	Consistency check via star counts . . . . .	17
3.3	Vertical structure of the Milky Way disk from RAVE . . . . .	18
3.3.1	Introduction . . . . .	18
3.3.2	Vertical velocity dispersion . . . . .	19
3.3.3	Gravitational potential of the disc . . . . .	19
3.3.4	Distribution over vertical energies . . . . .	20
<b>4</b>	<b>Horizontal structure of the disc</b>	<b>25</b>
4.1	Asymmetric drift and the local standard of rest . . . . .	25
4.1.1	Introduction . . . . .	25
4.1.2	The velocity ellipsoid . . . . .	26
4.1.3	The asymmetric drift . . . . .	27
4.1.4	Metallicity dependence . . . . .	30
4.1.5	Discussion . . . . .	31

4.2	Rotation curve of the Milky Way . . . . .	34
4.2.1	Introduction . . . . .	34
4.2.2	Local density constraints . . . . .	35
4.2.3	Local rotational velocity . . . . .	35
4.2.4	Tracing the rotation curve with SEGUE and RAVE stars . . . . .	36
4.2.5	Power index of the rotation curve . . . . .	37
4.3	Rotation curves for 3-component density models . . . . .	38
4.3.1	Rotation curves for spherical density distributions . . . . .	39
4.3.2	Rotation curves for flattened potentials . . . . .	40
4.3.3	Bulge . . . . .	41
4.3.4	Disc . . . . .	43
4.3.5	DM Halo . . . . .	45
4.4	Fitting observed rotation curve of the Milky Way with a density model . . . . .	46
<b>5</b>	<b>Perspectives</b>	<b>49</b>
5.1	Distribution functions in the plane of the Milky Way disc . . . . .	49
5.1.1	Epicyclic approximation . . . . .	49
5.1.2	Precise integration of orbits in 2D with a flat rotation curve . . . . .	50
5.1.3	Power-law rotation curve . . . . .	53
5.2	Dynamical heating of the disc as a diffusion process . . . . .	56
5.3	Statistical methods for adjusting theoretical distribution functions to observational data . . . . .	58
5.3.1	General idea . . . . .	58
5.3.2	Treating observational errors . . . . .	59
5.3.3	Biased samples . . . . .	60
5.3.4	Error estimate . . . . .	62
5.3.5	Applications . . . . .	63
<b>6</b>	<b>Summary</b>	<b>65</b>
	<b>Bibliography</b>	<b>66</b>
	<b>Acknowledgements</b>	<b>69</b>

# List of Figures

2.1	Colour-magnitude diagram for the RAVE sample. Colour-coded is the density of stars per unit area of the diagram. Black lines mark the adopted boundaries of the main sequence. . . . .	10
2.2	Colour-magnitude diagram for the Hipparcos sample. . . . .	10
2.3	Colour-magnitude diagram for the SEGUE G-dwarfs. . . . .	11
2.4	Colour-magnitude diagram for the SEGUE G-dwarfs in 2MASS colours. Density of stars with $0.48 < g - r < 0.55$ is colour coded, stars with $0.4 < g - r < 0.48$ are marked with brown dots, and stars with $0.3 < g - r < 0.4$ with blue dots. . . . .	12
2.5	Distribution of the SEGUE G-dwarfs in the $[\alpha/\text{Fe}]$ vs. $[\text{Fe}/\text{H}]$ plane. The two black lines present borders between the thin disc (below the lower line), the intermediate region (between the lines), and the thick disc (above the upper line), as they were determined by Lee et al. (2011). . . . .	12
2.6	Colour-magnitude diagram for the SEGUE M-dwarfs in the SEGUE $g$ and $r$ colours. . . . .	13
2.7	Colour-magnitude diagram for the SEGUE M-dwarfs in $J$ and $K$ colours. . . . .	14
3.1	Velocity dispersion as function of height for different color bins, each 50 pc wide. RAVE, Hipparcos and SEGUE data are used. . . . .	19
3.2	Velocity dispersion as function of height for different color bins. The height bin scans over $z$ . The first point in the plot contains 100 stars, then the number of stars increases, and reaches 400 at the second point with error bars. Then it is 400 all the time up to the third point with error bars, after which the limiting condition is the width of the bin, which is not greater than 100 pc. The smooth lines are predictions of Just & Jahreißmodel. . . . .	20
3.3	Estimates for the free fall acceleration as a function of height. The SEGUE sample is treated with Eq. 3.2, for the RAVE sample Kolmogorov-Smirnov test is used. . . . .	21
3.4	Distribution over vertical energies. . . . .	22
3.5	Distribution over vertical energies. . . . .	22
3.6	Distribution over vertical energies. . . . .	22
3.7	Distribution over vertical energies. . . . .	23
3.8	Distribution over vertical energies. . . . .	23
4.1	Properties of the velocity ellipsoid from the RAVE data. The upper panel shows the radial velocity dispersion as a function of colour. The second and the third panels present squared axis ratios of the velocity ellipsoid $\sigma_\phi^2/\sigma_R^2$ and $\sigma_z^2/\sigma_R^2$ as a functions of $\sigma_R^2$ with the median values marked by horizontal lines. The bottom panel shows the vertex deviation $\alpha$ of the velocity ellipsoid. . . . .	28

4.2	The asymmetric drift for different data sets. The two black circles on the $\Delta V$ axis correspond to the different local standards of rest with $V_{\odot} = 5.25 \text{ km s}^{-1}$ from Aumer & Binney (2009) and $V_{\odot} = 12.24 \text{ km s}^{-1}$ from Schönrich et al. (2010), respectively. The grey line gives the best fit to the data points for RAVE dwarfs. It corresponds to the LSR $V_{\odot} = 4.37 \text{ km s}^{-1}$ and the scalelength of the disc $R_d = 2.27 \text{ kpc}$ . . . . .	30
4.3	The asymmetric drift for the RAVE dwarfs separated into three metallicity bins: $-0.6 < [M/H] < -0.3$ , $-0.3 < [M/H] < -0.1$ , and $-0.1 < [M/H] < 0.1$ . The two black circles on the y-axis correspond to the LSR from Aumer & Binney (2009) and from Schönrich et al. (2010). The full lines show the best joint linear fit. Top: Using Eqn. (4.2). Bottom: Using Eqn. (4.5). . . . .	32
4.4	Rotation curve. . . . .	37
4.5	Data of Sofue et al. (Sofue et al. (2009)) with different $V_0$ showing negligible influence inside $R < 1 \text{ kpc}$ . Dehnen bulges with different cusp slopes $\gamma$ , which match the maximum. . . . .	42
4.6	Exponential discs with fixed local surface density: variation of scale length and cutting out an inner hole by subtracting an exponential disc with reduced scale length $R_d/n$ and reduced central surface density $\epsilon$ (chosen to just avoid a negative $V_c^2$ of the disc at the centre. The last (pink) line shows the effect of a gas disc with twice the scale length, where $13M_{\odot}/\text{pc}^2$ of the local surface density of $47M_{\odot}/\text{pc}^2$ is attributed to the gas disc. . . . .	44
4.7	Plot of $V_c^2$ , where the components add up linearly: Effect of a hole in the exponential disc with respect to reproduce the strong decline around $R = 2 \text{ kpc}$ . The bulge is a Hernquist model with parameters as in figure 4.5 for $\gamma = 1.0$ . . . . .	45
4.8	DM halo with local density fixed to $\rho_{h,0} \approx 0.01M_{\odot}/\text{pc}^3$ . Isothermal models with different core radius and the effect of flattening. . . . .	46
4.9	DM halo with local density fixed to $\rho_{h,0} \approx 0.01M_{\odot}/\text{pc}^3$ . NFW model with different scale radius and flattening. Additionally the modified Hubble and the Burkert models are shown. . . . .	47
4.10	Plot of $V_c^2$ for different DM halo models with fixed local volume density and varying scale radius. . . . .	47
4.11	Plot of $V_c^2$ for bulge + disc models (no DM halo) with maximum local surface density and varying scale length. The model with a hole ( $R_d/3$ and $\epsilon = 0.8$ ) can in principle reproduce the inner rotation curve. . . . .	48
4.12	Plot of $V_c^2$ for bulge + disc + halo models. The bulge is a Dehnen model with $M_b = 1.8e10M_{\odot}$ and a scale radius of $a_b = 0.22 \text{ kpc}$ . The disc is an exponential disc with $R_d = 3.0 \text{ kpc}$ with a hole ( $R_d/3$ and $\epsilon = 0.4$ ). The total disc mass is $M_d = 4.3 \times 10^{10}M_{\odot}$ . . . . .	48
5.1	Theoretical disc surface density distribution in epicyclic approximation . . . . .	51
5.2	Theoretical distribution over velocities $V$ in epicyclic approximation . . . . .	51
5.3	Theoretical ratio of velocity dispersions in epicyclic approximation . . . . .	52
5.4	Theoretical disc surface density distribution for flat rotation curve . . . . .	53

---

5.5	Theoretical distribution over velocities $V$ for flat rotation curve . . . . .	54
5.6	Theoretical ratio of velocity dispersions for flat rotation curve . . . . .	54
5.7	Observed distribution over velocities $V$ from the RAVE data . . . . .	55
5.8	Shapes of the function $F(x)$ for different amounts of $\beta$ . . . . .	57



# List of Tables

1.1	Space-based astrometric surveys. . . . .	8
1.2	Spectroscopic surveys Turon et al. (2008) . . . . .	8
4.1	Properties of samples used for our analysis. . . . .	38
4.2	Rotation curves for different spherical density distributions. The first column presents name of the model, the second presents density $\rho$ as function of dimensionless radius $y = \frac{R}{a}$ , the third column gives squared circular velocity in Galactic plane as function of $y$ . . . . .	40
4.3	Rotation curves for different density distributions. The first column presents name of the model, the second presents density $\rho$ as function of dimensionless radius $m = \frac{1}{a} \sqrt{R^2 + \frac{z^2}{q^2}}$ , the third column gives squared circular velocity in Galactic plane as function of $y = \frac{R}{a}$ . . . . .	41



# 1

## Introduction

### 1.1 What it is all about

---

#### 1.1.1 What is the Galaxy?

The Universe looks differently on different scales. Seen as a whole at Gigaparsec scales it seems uniform, on Megaparsec scales it consists of voids, walls, and clusters of galaxies, on kiloparsec scales we see individual galaxies, on AU scales the visible Universe consists predominantly of stars, and on fm scales of baryons. From this point of view a galaxy is more or less any self-gravitating system with size of 30 pc to 100 kpc. (Finding a more rigorous definition appears to be much more tricky: it is difficult to distinguish dwarf galaxies from globular clusters, and setting a limit when two merging galaxies turn into one is just a question of terminology.)

The galaxy containing the Solar system is called the Milky Way, or simply the Galaxy. It is a spiral galaxy consisting of some 100 billion stars, with a disc radius about 15 kpc, embedded into a dark matter halo extending to over 100 kpc.

#### 1.1.2 What the Galaxy is not?

Two important features of the Galaxy distinguishing it from many other physical and astrophysical systems are worth mentioning.

*The Galaxy is not stationary.* Two-body relaxation timescale is orders of magnitude longer than the age of the Galaxy. That is why relaxation mostly occurs through processes involving slight global perturbations of the gravitational potential. These processes are capable of substantially changing the structure of the Galaxy over cosmological timescales, but are way too slow to lead it to a quasiequilibrium thermodynamic state. (Moreover, the very idea of thermodynamical equilibrium can't be applied to a system consisting of self-gravitating particles.) The Galaxy as we see it thus presents a transient phenomenon, constantly being in the course of its formation.

*The Galaxy is not closed.* There is a stereotype, that astronomers mostly occupy themselves with closed systems, which can be well separated from the environment. This notion largely holds for stellar and planetary astronomy, planet dynamics, and cosmology (the Universe is closed by definition!), but totally breaks for the Galaxy. The Galaxy strongly interacts

with its environment, accreting intergalactic gas and merging with smaller galaxies, swallowing their stars and dark matter, and being dynamically perturbed by them.

### 1.1.3 Why study the Galaxy?

There is no practical need to study the Galaxy at all. Probably, galactic astronomy is the least practical branch of astronomy at all. Indeed, planetary science will probably acquire practical implications in the following centuries. Stellar astrophysics is at least important for understanding solar activity and predicting supernova explosions in the solar neighbourhood. Cosmology and studies of exotic astrophysical objects can have an impact on fundamental physics. On the other hand, interstellar spaceflights are so unrealistic, and the possible impact of galactic astronomy on the revelation of the structure of dark matter is so far-fetched, that we must recognize, that the practical outcome of the Galactic studies is almost nil.

But interests of fundamental science are not more deducible to practical necessities, than haute couture trends are deducible to the primary purpose of cloth to warm the body. And, similarly to fashion trends, trends of science demonstrate bold changes, which sometimes have deep reasons for them, and sometimes look just random. The very origination of galactic astronomy provides a magnificent example of such a change. When Messier composed his catalogue of nebulous objects, many of which later appeared to be external galaxies, he had a primary purpose to select all dull objects on the sky not to confuse them with comets, which really were interesting. Now the interests of scientists have changed drastically, and astronomers are investing galaxies with much more effort than comets.

Still, however interests of scientists changed over time, two questions always retained a great popularity: Where do we come from? and What constitutes the world? Up to our current understanding, the answer to the first question includes cosmology, galactic astronomy, star formation, planet formation, planetary science, and evolution biology, while the answer to the second question includes cosmology, galactic astronomy, stellar astronomy, planet formation, planet science, chemistry, molecular, atomic, nuclear, and particle physics, and deeper theories yet under construction. Understanding the Galaxy possesses an important place in both answers, and it makes a good excuse to study it. At least, the best one I can find for myself.

### 1.1.4 How study the Galaxy?

The Galaxy is a very complex system. Its physics involves a great variety of physical processes, including gravitational  $N$ -body problem of stellar dynamics, physical kinetics of dark matter, magnetohydrodynamics of star formation and supernova explosions, thermodynamics and nuclear physics that determine properties of stars. This makes it unrealistic to obtain a self-consistent theoretical derivation of properties of the Galaxy from first principles.

Numerical simulations of this problem as a whole are also not viable because of a great variety of spatial and temporal scales involved. Indeed, such a rigorous numerical model must include the entire Galactic halo ( $\sim 10^{22}$  m), but still resolve stellar sizes ( $\sim 10^9$  m) to account properly for the physics of star formation and supernova explosions, must include the entire age of the Galaxy ( $\sim 3 \cdot 10^{17}$  s), but still resolve timescales of individual supernova explosions

( $\sim 1$  s).

To be able to study the Galaxy, astronomers separate the simulation into smaller steps, which are simpler in terms of complexity for the analytical treatment and the required computational capabilities for numerical simulations. Thus star formation and supernova explosions are simulated on small scales, dynamics of star clusters on bigger scales, stellar dynamics and gas dynamics on even bigger scales, and everything is embedded into a dark matter halo, which is simulated on the largest scales. Outcomes of some simulations are taking as prerequisites to others, and ideally they all have to become consistent in the end. The situation is similar to cartography, where it is impossible to depict the entire Earth in one map, so one has to make different maps for different parts of the Earth's surface and to conjugate them, checking that overlapping maps depict the same areas consistently.

The primary topic of this thesis is stellar dynamics of the Galactic disc. This implies distance scales from roughly 0.1 to 10 kpc and time scales from roughly 0.1 to 10 Gigayears. At these scales the number of stars is so large, that the Galaxy is seen as a continuous medium. The stars are moving in the collective potential created by the dark matter halo, the interstellar gas, and the stars themselves.

## 1.2 Formation of the Galaxy

---

The Milky Way was formed in cosmological context from an almost uniform distribution of baryonic and dark matter. Primordial density fluctuations in the early Universe grew through Jeans instability, creating dark matter halos, that merged with each other, forming ever more massive structures. Baryonic gas, distributed between these halos, gradually radiated away its energy, cooled down and sank to the centres of potential wells of the halos. Dark energy didn't have such effective mechanisms to loose its random motion, and baryonic matter compressed far below the size of the dark matter halo. But in the course of this compression it conserved a large fraction of its initial angular momentum, that in some cases led to formation of rotating discs of baryonic gas. Further cooling down, the gas formed cold molecular clouds, Jeans instabilities governed star formation, while spiral and bar instabilities created prominent patterns in the disc. Material processed in stars and released by supernovae explosions is used again for star formation, this time allowing to form planets around stars.

Alternative theories of gravity, the most notably Modified Newtonian dynamics (MOND), compete with the standard cosmological model  $\Lambda$ CDM in the description of the process of galaxy formation, but up to now  $\Lambda$ CDM seems to be the simplest and the best consistent with the bulk of cosmological and astrophysical data. Simulations of structure formation in cosmology nicely agree with observations (Springel et al. (2005)), and simulations of structure of a separate galaxy succeed to reproduce most basic features (Scannapieco et al. (2012)). Some contradictions still persist (dwarf satellite problem, cuspy halo problem, too massive bulges in most numerical simulations), but they may be soon solved by better accounting for astrophysical processes in baryonic matter, a better resolution of simulation or even a different interpretation of observational data. The flows of the theory are overwhelmed by its successes, and it is an outstanding case in astronomy when a theory with such a small number of free

parameters can explain results of so many different observations.

The unclearness of nature of dark matter and dark energy is an origin of constant worry. The most popular candidates for dark matter are Weakly Interacting Massive Particles (WIMPs) or axions, while the origin of dark energy is usually sought among scalar fields. But their exact nature appears to be almost unimportant for cosmology. The only property of dark energy that matters is constancy of its density, while for dark matter the essential properties are its coldness (speeds of particles are much less than speed of light), darkness (no essential interaction with electromagnetic radiation), and constancy of its mass (density inversely proportional to the scale factor cubed). This allows cosmologists to build a phenomenological theory, applicable for whatever the exact nature of dark matter and dark energy is.

## 1.3 Structure of the Galaxy

The Milky Way is a barred spiral galaxy of type SBc. It can be conveniently separated into a halo, a bar/bulge, and a disc.

### 1.3.1 The halo

The dark matter halo has a mass of about  $(1 \div 1.5) \times 10^{12}$  (McMillan (2011)), comprising the major contribution to the total mass of the Galaxy. There are no direct ways to observe structures in the distribution of the dark matter, but numerical simulations prove the dark matter halo to be very clumpy, including a number of tidal streams, subhalos and subsubhalos in different phases of their accretion and dissolution.

Halo stars are not essential in terms of their total mass, but serve as important tracers of structures in the halo and of the history of the Galactic environment. They all are metal-poor, demonstrate no net rotation or a slight rotation in the negative direction. Their mean density is close to a power law  $\rho \propto r^{-2.8}$  (Turon et al. (2008)).

Embedded in the halo are globular clusters and satellite galaxies, that have a whole branch of interesting astrophysics, but their consideration goes far beyond the scope of this thesis.

### 1.3.2 The bulge

The bulge dominates density of the Milky Way inside  $\sim 1$  kpc. It is geometrically and chemically complex, with its main body being barred, gas-poor, and consisting of old stars, while its inner parts are gas-rich and demonstrate active star formation. The bar rotates with a pattern speed about  $19 \text{ Gyr}^{-1}$  (Dehnen (1999)), its orientation changes when moving towards the centre (Nishiyama et al. (2005), Gonzalez et al. (2011)), that is attributed to the existence of an inner bar, having a length about 1 kpc and being nearly perpendicular to the line of sight.

In the centre of the bulge a supermassive black hole is situated, with a mass of  $M_{\text{MBH}} = (4.30 \pm 0.20)_{\text{stat}} \pm 0.30_{\text{sys}} \times 10^6 M_{\odot}$  (Gillessen et al. (2009)). It is associated with the radio source Sgr A\*.

### 1.3.3 The disc

The disc extends to the radius of about 15 kpc, with the Sun lying at about 8 kpc from the centre. The disc is separated into a thin disc (metal-rich, alpha-weak, low velocity dispersion, scale height  $\sim 300$  pc) and a thick disc (metal-poor, alpha-strong, high velocity dispersion, scale height  $\sim 900$  pc). It is still an open question whether there is a real dichotomy between these two populations (Lee et al. (2011)) or a smooth transition from one population to the other (Bovy et al. (2012)). The thin disc is found to form spiral arms, but the shape and the number of arms is still discussed. Outside the solar radius the disc is warped.

## 1.4 Stellar dynamics

The major contribution to the gravitational potential of the Galaxy is presented by mean densities of dark matter, stars, and gas. It makes sense first to consider motion of a star in this smooth potential, and then to treat inhomogeneities of the potential as perturbations superimposed on the idealized motion in the smooth potential.

The smooth potential is axi-symmetric, therefore angular momentum  $L_z$  is conserved in this motion. The total energy  $E$  is another conserved quantity. Two integrals of motion are not enough to constrain a 3-dimensional orbit, but simulations show, that the third integral of motion exists, even though it can not be expressed analytically. If a star is on a nearly circular orbit with only small vertical and radial excursions, vertical and horizontal motion decouple, and a good approximation to the three integrals of motion is given by the vertical energy  $E_z$ , the effective radial energy  $E_R$ , and the angular momentum  $L_z$ . Doing Taylor decomposition of  $E_R$  over small radial excursions of the star one gets the epicyclic approximation of its motion. In this approximation the star appears to rotate around an ellipsis (epicycle), while the centre of epicycle (guiding centre) is uniformly rotating around the Galactic centre. The distance from the guiding centre to the centre of the Galaxy  $R_g$  (guiding radius) is defined by the angular momentum  $L_z$ , and the rotational velocity of guiding centre is just circular velocity of the Galaxy at the guiding radius  $V_c(R_g)$ . The shape of the epicycle is defined by the slope of the rotation curve of the Galaxy at radius  $R_g$ , its size depends on the effective energy  $E_R$ , and the frequency of the rotation around this ellipsis  $\kappa$  is independent of  $E_R$ . In the meantime the star is doing vertical oscillations around the Galactic plane with a different frequency  $\nu$ . When we add all these motions together, in 3 dimensions we shall get a trajectory, confined to a torus of rectangular cross-section, which in general (if there are no co-measurabilities between frequencies) fills the ring. If radial or vertical excursions of a star are big, epicyclic approximation is no longer valid, and, moreover, radial and vertical motions are no longer decoupled. The orbit acquires a more complex shape, but is still constrained to some torus, and still characterized by three integrals of motion.

If perturbations are superimposed on this regular motion of a star, the star still can be thought as moving almost along this unperturbed orbit in any instant of time, but parameters characterizing this orbit slowly change with time. The three main sources of perturbations are known, but their relative importance is still under debate:

*Clumps of dark matter.* Simulations of galaxy formation show that dark matter halos of

galaxies are clumpy and rich in substructures, including partially dissolved halos of formerly accreted satellites, tidal streams, and satellites currently in the course of accretion. Gravitational interaction with these substructures can perturb regular motion of stars.

*Transient structures in the disc.* A periodical spiral pattern can cause secular perturbations only in resonances. But if the spiral structure is transient, it can in principle dynamically heat populations of stars at all locations with heating rate depending on current orbit of the star. This mechanism appears to work more effectively for heating in the plane of the disc, than in the vertical direction.

*Molecular clouds.* Stars are scattered by massive molecular clouds. As velocities of molecular clouds with respect to the local standard of rest are relatively small, stars probably do not gain much energy in these collisions. But they are thought to be very important for pumping energy from motion in the plane of the disc to the vertical motion.

Stars form in massive molecular clouds, who possess almost circular orbits. That is why young stars also have small vertical and epicyclic energies. Eventually their orbits get perturbed, and stars increase their epicyclic and vertical energy. Later orbits of stars get so non-circular, that it makes no sense to speak about epicyclic approximation and about vertical energy. Action-angle variables are the best way of general description of such orbits. They are especially convenient for studying small perturbations of regular motion. But the problem is that actions can be expressed analytically only in few special cases. Any realistic gravitational potential of the Galaxy leads to complicated numerical computations.

## 1.5 Surveys of the Galaxy

---

To study stellar dynamics in the Galaxy one needs large ensembles of stars with the whole 6D dynamical information (3 coordinates and 3 velocity components), and preferentially also with metallicities, chemical compositions, and ages. Biases in these samples are strongly unwanted, and volume-complete samples are the best ones.

Let's discuss obtaining these 6 dynamical components in more detail.

1. *Angular coordinates* do not have to be measured too precisely: for the sake of dynamical modelling errors of arcseconds and even arcminutes are still tolerable. We have angular coordinates with arcsecond precision for billions of stars, and these 2 coordinates never become a limiting factor.

2. *Proper motions* of stars are also measured astrometrically, by comparing the position of a star on the celestial sphere in two different epochs. And in this case a much more precise astrometry is needed. For example, to measure proper motion of a star at 1 kpc with 10% accuracy by comparing its positions in two epochs separated by 10 years, a milliarcsecond accuracy is needed, which is already very complex for ground-based observations. Nevertheless, proper motions are known for millions of stars (most notably, Tycho-2 catalogue with 2 539 913 stars), and they also do not strongly constrain Galactic studies.

3. *Line-of-sight velocity* can only be determined spectroscopically, from Doppler shift spectroscopy. As spectroscopy usually requires longer exposures than astrometry, and the number of targets observed simultaneously is limited to some hundreds, spectroscopic surveys

appear to be very time-costly, and availability of spectroscopic data presents a major constraint for stellar samples. Up to now RAVE with 600 000 stars and SDSS with 250 000 stars are the most extended surveys of this sort. LAMOST, which has recently started in China, is expected to supercede them in the term of number of stars.

4. *Distances* to field stars in the Galaxy are the most commonly produced by measurements of parallaxes and by fitting stellar models to spectroscopic data. For pulsating stars distances can be determined from period-luminosity relation. Distances to stellar clusters can be obtained by fitting Hertzsprung-Russell diagram.

Measurements of parallaxes can be easily performed for the nearest stars, but measuring parallaxes of more distant stars requires very accurate astrometry. For example, to measure the distance to a star lying at 1 kpc with 10% accuracy by parallax method, its position must be measured with precision  $100 \mu\text{as}$ . This precision is available for space telescopes only. Hipparcos mission that operated between 1989 and 1993 still represents state of the art in this field, with the resulting catalogue including 118 000 stars. Gaia mission, that is expected to be launched in September 2013, should provide  $10^9$  parallaxes. Gaia should also provide high-resolution spectroscopy in a narrow band 847-874 nm for stars up to 17th magnitude, thus measuring their line-of-sight velocities.

Fitting stellar models to observational data is another important method of measuring distances to stars. It works as follows. Photometrically we can measure apparent magnitudes of a star in different filters, spectroscopically we can also determine its metallicity  $[\text{Fe}/\text{H}]$ , alpha-abundance  $[\alpha/\text{H}]$ , temperature  $T$ , logarithm of the free-fall acceleration on the surface  $\log g$ . All these properties can be in principle deduced with a high accuracy from its age  $t$ , initial mass  $M$ , metallicity  $[\text{Fe}/\text{H}]$ , alpha-enhancement  $[\alpha/\text{Fe}]$ , distance  $r$ , and reddening. Other properties (like angular momentum, magnetic field, detailed elemental abundance) are usually much less important, so that we can assume the 7-9 observables (depending on number of filters) to be functions of 5-6 free parameters (depending on whether reddening is used as a free parameter). These functions are known with good accuracy from theories of stellar evolution and from local samples. If the number of observables is bigger than the number of free parameters, we can choose parameters to fit the observations, and thus determine all free parameters including the distance. In reality some degeneracies arise. For example, stars do not strongly change their properties during their main sequence phase, and therefore determining stellar age by this method is subjected to high uncertainties. Temperature and colours strongly correlate, thus adding more magnitudes in different filters usually does not help to improve the accuracy. In particular, it is almost impossible to do a reliable fitting having only photometry in different filters, without spectroscopy: spectroscopically determined  $\log g$  is a key probe to distinguish dwarfs from giants. But having intermediate-resolution spectroscopy with signal to noise ratio above 20 usually allows to do the fitting and to get distances with uncertainties of order of 30%. This work was done for RAVE stars (Zwitter et al. (2010), Breddels et al. (2010)) and SDSS stars (Lee et al. (2011)).

Table 1.1: Space-based astrometric surveys.

Name	Years	Number of parallaxes	V-magnitude	$\sigma_{\pi}$ , [ $\mu\text{as}$ ]
Hipparcos	1989-1993	118 000	2-12.4	4000-200
Gaia	2013-2019	$10^9$	6-20	200-20

Table 1.2: Spectroscopic surveys Turon et al. (2008)

Name	Years	Number of stars	Magnitude	Wavelength [ $\mu\text{m}$ ]	Resolution
RAVE	2003-2013	600 000	9-12 ( <i>V</i> )	0.84-0.88	7500
SEGUE	2005-	250 000	14.5-20.5 ( <i>g</i> )	0.38-0.92	2000
LAMOST	2011-			0.39-0.90	2500
APOGEE	2011-2014	100 000	<12.5 ( <i>H</i> )	1.52-1.69	20 000

## 1.6 State of the art

The local standard of rest in the Galaxy was established using Hipparcos data. Dehnen & Binney (1998) assumed linear dependence of the mean rotational velocity of a stellar sample on its velocity dispersion (Strömberg's relation), and the velocity of the Sun in the direction of the Galactic rotation with respect to the LSR appeared to be  $V_{\odot} = 5.25 \pm 0.62 \text{ km s}^{-1}$ . This result considered to be well established for a decade (Aumer & Binney 2009), until the underlying assumption of this analysis was questioned by Schönrich et al. (2010), who got  $V_{\odot} = 12.24 \pm 0.47 \text{ km s}^{-1}$ . This controversy is very important, as changing the local standard of rest will influence all the data analysis of stellar samples, and thus change the measured rotation curve of the Galaxy, radial scalelength of the disc etc. Also the applicability of the linear Strömberg's relation to the Milky Way disc is an important question, probing the history of star formation and dynamical heating.

# 2

## Data analysis

### 2.1 Used data sets

---

#### 2.1.1 RAVE

The RAVE sample we are using is an extended version of the sample discussed in Zwitter et al. (2010). It includes 222 241 stars with distance estimates, radial velocities and proper motions. Errors in distances, radial velocities and proper motions are also estimated.

Figure 2.1 presents CMD of the sample in  $J - K$  colours. For our analysis we select the main sequence according to the criterion  $5(J - K) < J < 5(J - K) + 2$ . The borders of the main sequence are plotted with two black lines in Fig. 2.1. Then we separate the main sequence stars into 5 bins according to their colours:  $0.1 < J - K < 0.2$ ,  $0.2 < J - K < 0.3$ ,  $0.3 < J - K < 0.4$ ,  $0.4 < J - K < 0.5$ , and  $0.5 < J - K < 0.9$ .

#### 2.1.2 Hipparcos

The sample from Anderson & Francis (2012) contains 116 096 stars with the Hipparcos parallaxes. We exclude stars, which are marked as group or cluster members, or as components of multiple stellar systems. To have a sample without velocity biases, we exclude stars with  $V$  magnitude bigger than 7.3. We also exclude stars with negative parallaxes, with absolute distance errors bigger than 0.2 with velocity error 7.5 km/s or bigger, or without  $J$  and  $K$  photometry. Thus we end up with 9 590 stars.

Their CMD is presented in Fig. 2.2. We adopted the same boundaries of the main sequence and performed the same binning in  $J - K$  colour, as we did for RAVE.

#### 2.1.3 SEGUE G-dwarfs

We use a sample of G-dwarfs and subgiants presented by Lee et al. (2011). The sample contains distance estimates for 40 496 stars. Following Lee et al. (2011), we use only stars with  $d < 3$  kpc,  $\log g \geq 4.2$ ,  $S/N \geq 30$ ,  $[Fe/H] > -1.2$ . The residual sample contains 20 141 stars.

The CMD of the sample is presented in Fig. 2.3.

We cross-match the sample with 2MASS point-source catalogue. Most stars of the sample still have 2MASS photometry, but as SEGUE stars are at the faint end of 2MASS magnitude range, the  $J$  and  $K$  magnitudes from 2MASS catalogue have high errors, mostly about 0.1

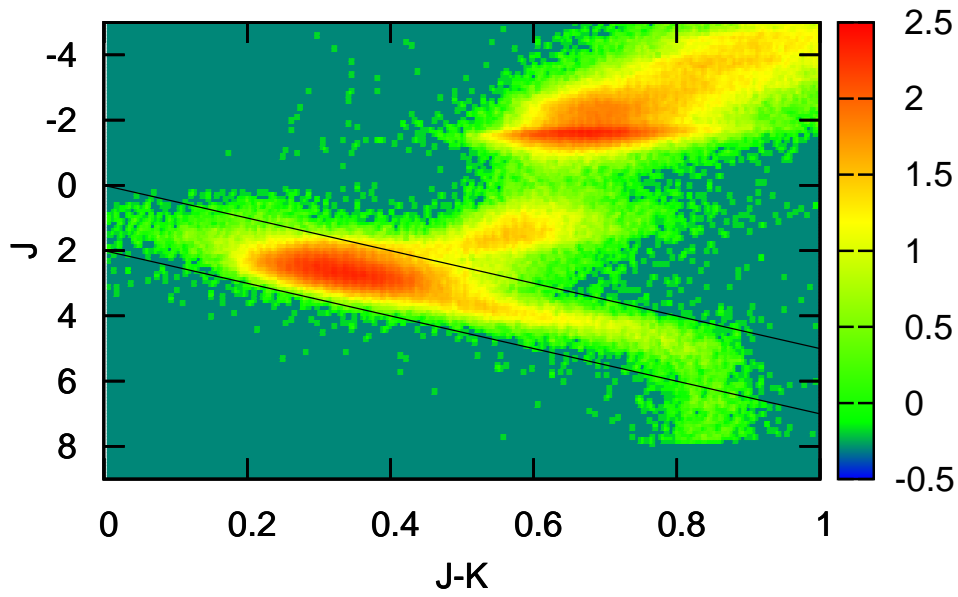


Figure 2.1: Colour-magnitude diagram for the RAVE sample. Colour-coded is the density of stars per unit area of the diagram. Black lines mark the adopted boundaries of the main sequence.

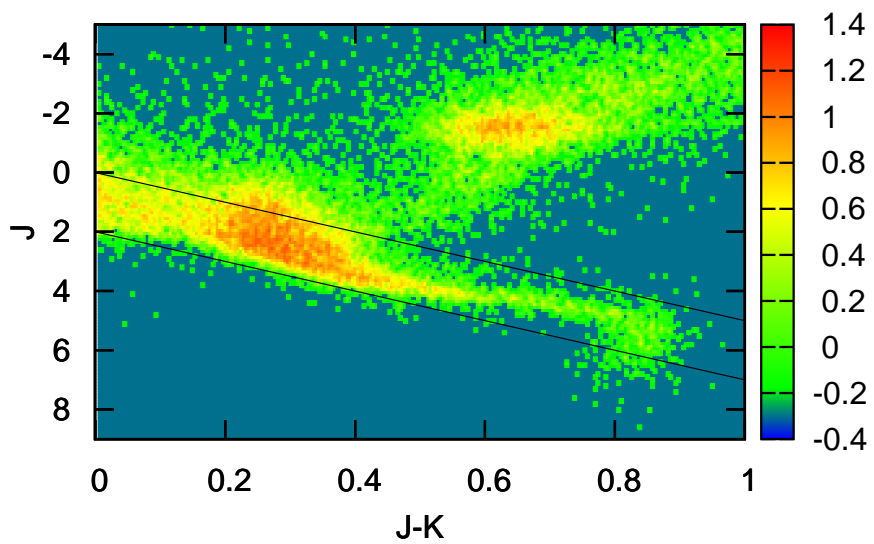


Figure 2.2: Colour-magnitude diagram for the Hipparcos sample.

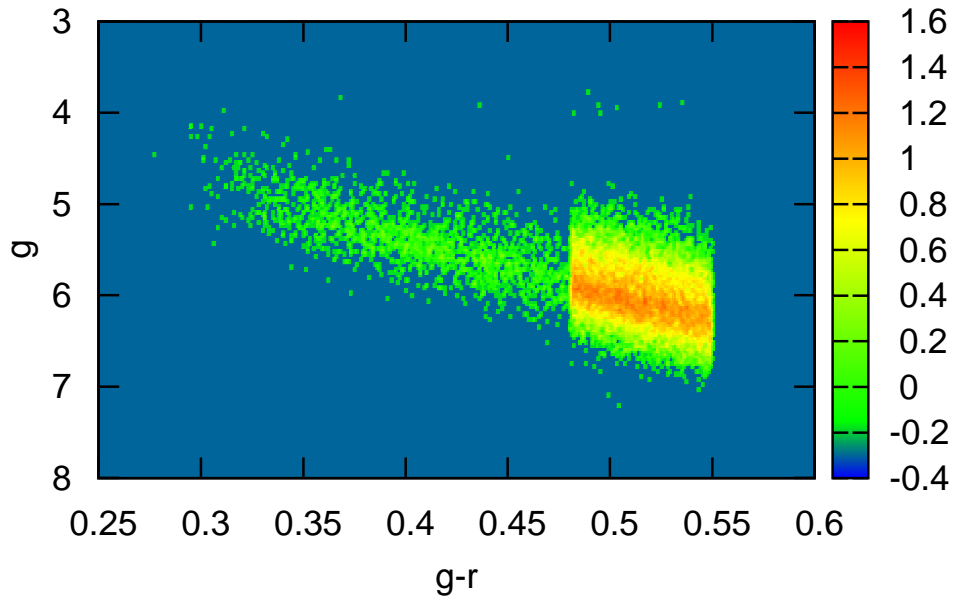


Figure 2.3: Colour-magnitude diagram for the SEGUE G-dwarfs.

mag in each colour. The CMD in  $J$  and  $K$  colours is presented in Fig. 2.4. Stars are separated into 3 bins according to their  $g - r$  colours, and the bins are plotted in different way: density of stars belonging to the most abundant bin with  $0.48 < g - r < 0.55$  is colour coded, stars with  $0.4 < g - r < 0.48$  are marked with brown dots, and stars with  $0.3 < g - r < 0.4$  are marked with blue dots. The spread of stars within each bin is consistent with the errors in  $J$  and  $K$  colours, while systematic offset between the bins consistent with the trend of the main sequence is also present.

In Fig. 2.5 we plot the distribution of the stars in the  $[\alpha/\text{Fe}]$  vs.  $[\text{Fe}/\text{H}]$  plane. The two black lines present borders between the thin disc (below the lower line), the intermediate region (between the lines), and the thick disc (above the upper line), as they were determined by Lee et al. (2011).

#### 2.1.4 SEGUE M-dwarfs

The sample contains 70841 SEGUE M-dwarfs from West et al. (2011). We exclude suspected white dwarf - M dwarf pairs (flag "WDF" equals 1), stars with bad photometry (flag "GOODPHOT" equals 0), stars with bad proper motions (flag "GOODPM" equals 0), and stars without line of sight velocities. Thus we end up with 38862 stars.

For these stars we have distance estimates and radial velocity measurements (without error estimates), proper motions with errors, SDSS  $ugriz$  photometry corrected for extinction by Schlegel maps. Most stars also have  $JHK$  photometry. Figure 2.6 presents CMD of the sample in  $g - r$  colours, and Fig. 2.7 in  $J - K$  colours. (For both plots only stars with errors smaller than 0.05 mag in corresponding colours were selected.) In  $J$  and  $K$  magnitudes the sample

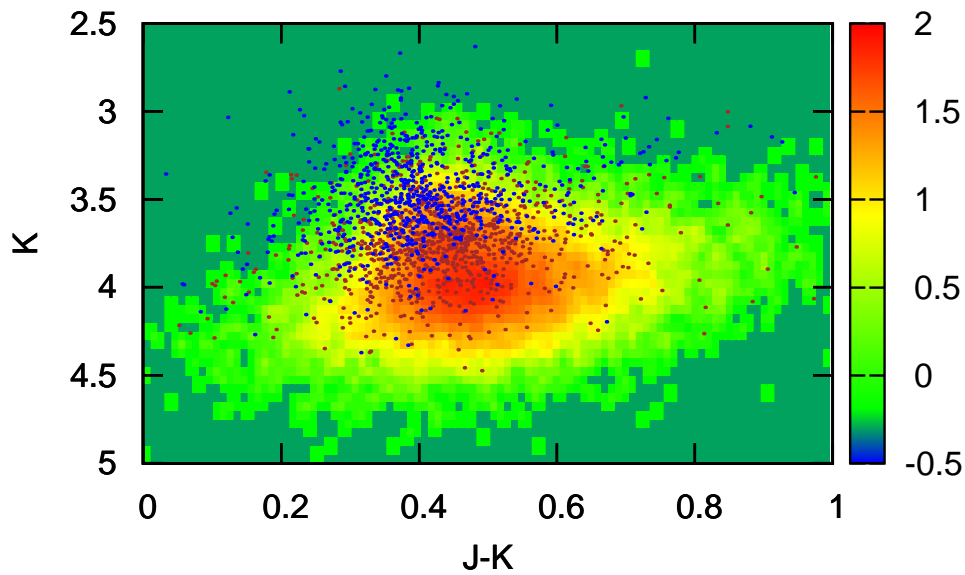


Figure 2.4: Colour-magnitude diagram for the SEGUE G-dwarfs in 2MASS colours. Density of stars with  $0.48 < g - r < 0.55$  is colour coded, stars with  $0.4 < g - r < 0.48$  are marked with brown dots, and stars with  $0.3 < g - r < 0.4$  with blue dots.

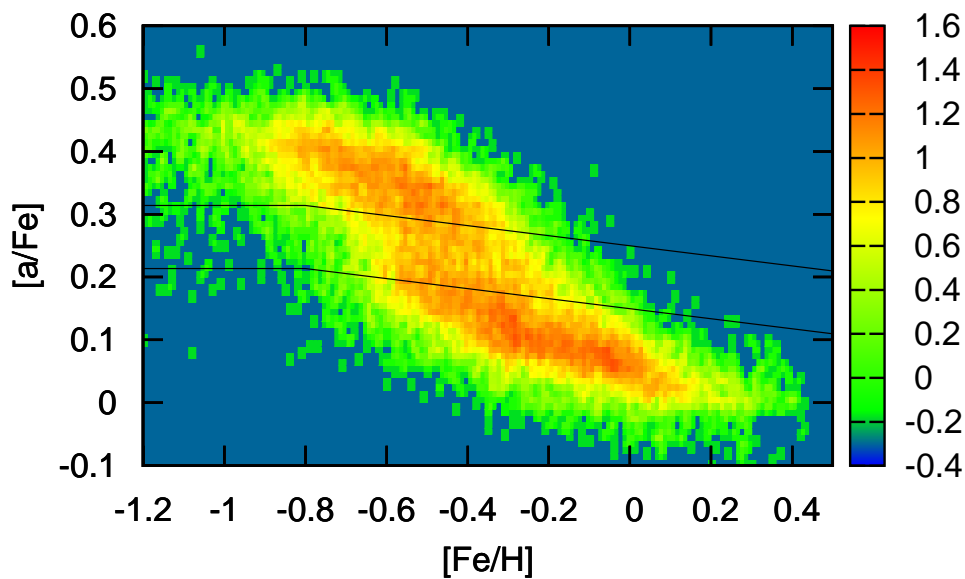


Figure 2.5: Distribution of the SEGUE G-dwarfs in the  $[\alpha/\text{Fe}]$  vs.  $[\text{Fe}/\text{H}]$  plane. The two black lines present borders between the thin disc (below the lower line), the intermediate region (between the lines), and the thick disc (above the upper line), as they were determined by Lee et al. (2011).

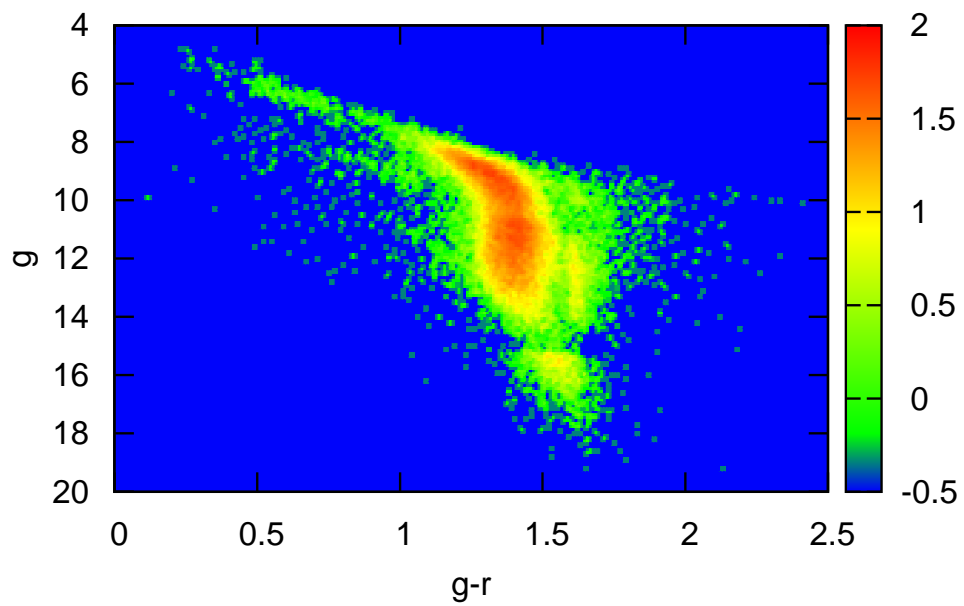


Figure 2.6: Colour-magnitude diagram for the SEGUE M-dwarfs in the SEGUE  $g$  and  $r$  colours.

occupies the proper place for M-dwarfs, while in  $g$  and  $r$  colours some stars look like K and even G dwarfs.

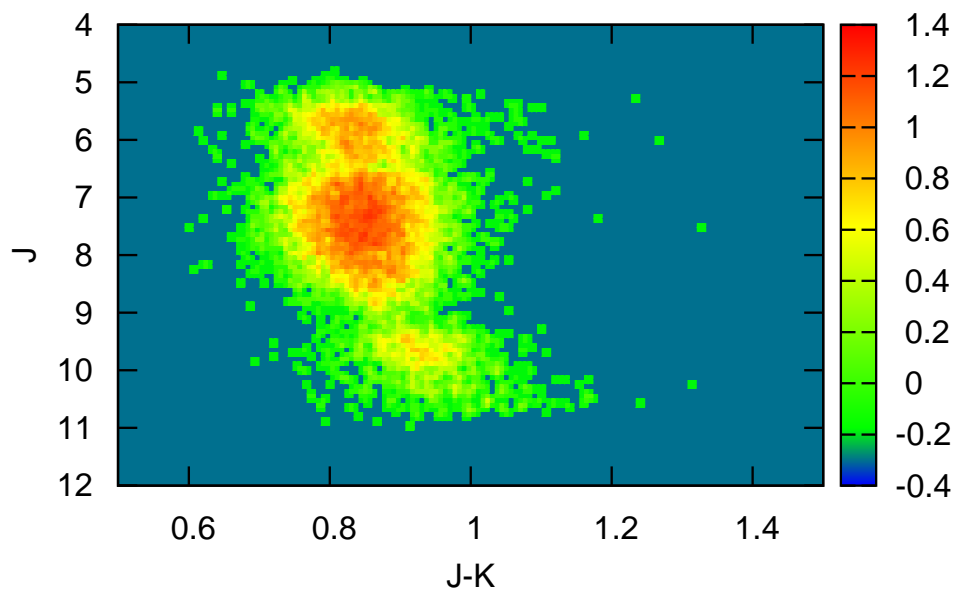


Figure 2.7: Colour-magnitude diagram for the SEGUE M-dwarfs in  $J$  and  $K$  colours.

## 2.2 Rotation curve data

### 2.2.1 Observations of the rotation curve

The inner rotation curve can be reliably measured by HI tangent point method. An advantage of this method is that it doesn't rely on distance estimates to the tracers. The method can not be applied for the outer rotation curve, and distance estimates are needed there.

In the last decades various methods have been applied to obtain rotation curve outside solar radius. Fich et al. (Fich et al. (1989)) compiled a catalogue of distances to HII regions and their line-of-sight velocities, and used the catalogue to construct rotation curve outside solar radius. Honma & Sofue (Honma & Sofue (1997b), Honma & Sofue (1997a)) obtained rotational velocities from the HI-disc thickness method. Nakashima et al. (Nakashima et al. (2000)) used C- and O-rich SiO maser emission Miras to trace rotation of the outer disc. Demers & Battinelli (Demers & Battinelli (2007)) used C stars as kinematic probes of the Milky Way disc. Frinchaboy & Majewski are conducting a long-term project of open clusters velocity and distances determination with the aim to use them as the disc tracers. Some results of the project are already available (Frinchaboy & Majewski Frinchaboy & Majewski (2008)). Maciel & Lago (Maciel & Lago (2005)) derived the rotation curve from planetary nebulae. VLBI observations of water maser sources in star-forming regions conducted with VERA provided several very accurate points on outer rotation curve (Honma et al. (2007), Oh et al. (2010)).

### 2.2.2 Rescaling the data

We use for the standard of rest at galactocentric distance  $R_0$  the angular speed  $\Omega_0 = \Omega(R_0)$  and circular velocity  $V_0 = V_c(R_0) = \Omega_0 R_0$ . The line of sight velocity projected onto the Galactic plane  $V_r = V_{lsr} / \cos b$  is given by

$$V_r = R_0 [\Omega(R) - \Omega(R_0)] \sin l \quad (2.1)$$

leading to the rotation curve

$$V_c(R) = \frac{R}{R_0} \left( V_0 + \frac{V_r}{\sin l} \right) \quad (2.2)$$

The data of Sofue et al. (Sofue et al. (2009)) are scaled to the local standard of rest  $(R_n, V_n) = (8\text{kpc}, 200\text{km/s})$ . If we want to use a different LSR  $(R_0, V_0)$ , the data must be rescaled. As the initial data  $R$  and  $V_r$  are not available, we must use Sofue's circular velocity  $V_{sn}$  to find rescaled velocity  $V_c$ . Solvability of this problem depends on whether  $R$  is smaller or greater than  $R_0$ .

**Inner rotation curve** For the inner rotation curve determined by the tangent method we have  $|\sin l| = R/R_0$  leading to the simple equation

$$V_c(R) = V_0 \frac{R}{R_0} + |V_r| \quad (2.3)$$

Rescaling of the data to a different LSR set ( $f * R_0, V_0 + dV_0$ ) is simple using

$$R \rightarrow f R \quad V_c(f R) = V_c(R) + dV_0 \frac{R}{R_0} \quad (2.4)$$

The shape is independent of  $R_0$  and changing  $R_0$  by a factor  $f$  corresponds to rescaling the enclosed masses inside  $R/R_0$  by the same factor. Since the enclosed mass  $M_r(R_0)$  for the disc is proportional to  $\Sigma_0 R_d^2$ , the surface density would decrease by the same factor  $f$ . Volume densities (of bulge and halo) would decrease by the factor  $f^2$ .

**Outer rotation curve** For the outer rotation curve it is more complicated, because the galactocentric distance  $R$  must be determined by

$$R^2 = R_0^2 + r^2 - 2R_0 r \cos l \quad (2.5)$$

and the circular speed is

$$\begin{aligned} V_c(R) &= V_0 \frac{R}{R_0} + \frac{V_r}{\sin l} \frac{R}{R_0} = \\ &= \left( V_0 + \frac{V_r}{\sin l} \right) \sqrt{1 - 2 \cos l \frac{r}{R_0} + \left( \frac{r}{R_0} \right)^2} \end{aligned} \quad (2.6)$$

Rescaling to a different  $V_0$  is the same as for the inner rotation curve (it corresponds to a rigid rotation correction), but for a correction to a different  $R_0$  the distance  $r$  and Galactic longitude  $l$  must be used (known).

# 3

## Vertical structure of the disc

### 3.1 A self-consistent local disk model

---

Just & Jahreiß (2010) presented a new Galactic disc model (hereafter “Just-Jahreiß model”):

$$\rho_{s,j}(z) = \frac{g(\tau_j)\text{SFH}(t_j)dt}{2h_d(\tau_j)} \exp\left[\frac{-\Phi(z)}{\sigma_w^2(\tau_j)}\right]$$

where  $\rho_{s,j}$  is the density of the thin disk (component  $s$ ) with the age bin  $j$ , the  $g$  accounts for mass loss by stellar evolution, the thickness  $h_d$  and potential  $\Phi$  are determined iteratively via kinematics constrains. The thin disk is expressed using a continuous set of isothermal sub-populations with age range from 0 to 12 Gyr and the size of bins 25 Myr. The thick disk has a single population with the oldest component of 12 Gyr.

### 3.2 Consistency check via star counts

---

In Just et al. (2011) Just-Jahreiß model was compared with SDSS data at the Galactic pole field in order to constrain the SFR of the thin disc. The “model A” of Just-Jahreiß model demonstrated a good match of luminosity functions and Hess diagrams. The typical discrepancy of star counts in the color-magnitude diagram was less than 5 per cent. The total local star numbers determined from fitting data were in a reasonable agreement with local survey.

### 3.3 Vertical structure of the Milky Way disk from RAVE

We use RAVE 2 data to extract information about vertical structure of the Milky Way disc. Vertical velocity dispersion is studied as function of height. Comparison with the local velocity dispersion from Hypparcos implies either existence of sharp maximum of vertical velocity dispersion at the Galactic midplane or inconsistency of the two surveys. We discuss the possibility of such a maximum and the consequences it implies. We construct distribution of stars over energies of vertical motion for different subpopulations presented in the RAVE sample, and use it to predict stellar density distribution in the disc.

#### 3.3.1 Introduction

Observational programs of the last decades enormously expanded our knowledge of the Milky Way disk. These observations provided us with information about the distribution functions of stars in the Milky Way,  $f_i(R, \phi, z, u, v, w)$ , where  $R, \phi, z$  are cylindrical coordinates in the Milky way,  $u, v, w$  are velocity components, and  $i$  is the number of subpopulation. When speaking about vertical motion in the solar cilinder, as we do in this article, one is interested in  $f_i(z, w)$  only, where we substitute solar coordinates  $R$  and  $\phi$  and integrate over velocity components  $u$  and  $v$ . No survey has yet measured  $f_i(z, w)$  directly in all the domain of interest for the Milky Way disc studies. Hypparcos provided us with knowledge of velocity distribution in the solar neighbourhood,  $f_i(0, w)$ , but told nothing about large  $z$ . Starcounts from 2MASS could be used to get stellar density,  $\nu(z)$ , 0th velocity momentum of  $f_i(z, w)$ . RAVE provided cross-sections of  $f_i(z, w)$  for given  $z$ , but these cross-sections can't be put together due to unknown sampling function.

But  $f_i(z, w)$  is in some sense overabundant. In the case of dynamic equilibrium according to the Jeans theorem  $f_i(z, w)$  must be a function of integrals of motion, which in 1-dimensional case is the total vertical energy only. Thus set of distributions over energies  $f_i(E)$  for different subpopulations together with gravitational potential  $\Phi(z)$  contain all the information about vertical dynamics in the disc. The measured moments and cross-sections from the mathematical point of wiew are sufficient not only to constrain  $f_i(E)$  and  $\Phi(z)$ , but also to cross-check consistency of our assumptions (e.g. dependence of  $f_i$  of energy only, absence of biases in the measurements etc.). Even though in reality everything appears to be by far more complex due to observational and statistical errors in the samples, we already can find  $f_i(E)$  and  $\Phi(z)$  with ever better accuracy.

Functions  $f_i(E)$  and  $\Phi(z)$  are formed by many entangled factors.  $f_i(E)$  is determined by star formation rate, initial mass function and initial distribution over velocities, which are altered by dynamical heating and radial migration with the lapse of time.  $\Phi(z)$  in addition to stellar component is influenced by dark matter and gas components. Constraining  $f_i(E)$  and  $\Phi(z)$  from the observational data analys allows us to extract information about all these interfering factors, IMF and SFR, dynamical heating and radial migration, dark matter density and gas distribution in the disc, thus providing a tool to understand various aspects of the Galaxy formation and evolution.

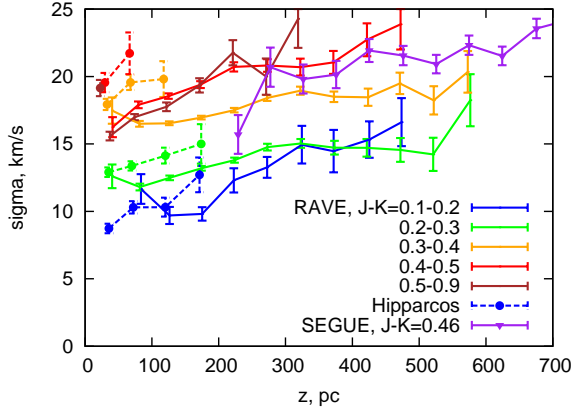


Figure 3.1: Velocity dispersion as function of height for different color bins, each 50 pc wide. RAVE, Hipparcos and SEGUE data are used.

### 3.3.2 Vertical velocity dispersion

We bin stars in 50 pc bins in height  $z$  and calculate velocity dispersion  $\sigma$  in each bin. Then we plot  $\sigma$  as a function of average absolute value of  $z$  in a bin (Fig. 3.1 and 3.2). The plotted error bars are purely statistical errors, without taking into account errors in  $W$ . The general trend of the curves is quite understandable. Redder stars have larger main sequence lifetime, and are thus in average older, demonstrating higher velocity dispersion. Farther from the Galactic midplane fraction of young dynamically cold stars goes down, and old dynamically hot population dominates, causing larger  $\sigma$  than for small  $|z|$ . For large  $|z|$  velocity dispersion must presumably tend to limiting value, that corresponds to the velocity dispersion, which can be reached in the course of main sequence life time of stars in a given colour bin. The limiting value is generally larger for redder stars as their main sequence lifetime is larger. But it is the same for the last two colour bins, because for them main sequence lifetime is larger than the age of the Galaxy.

### 3.3.3 Gravitational potential of the disc

In the SEGUE sample we have two distinct populations (alpha-strong and alpha-weak) with nearly the same velocity biases, but different kinematics. Each of the populations obeys Jeans equation,

$$\frac{d \ln v_{1,2} \sigma_{1,2}^2}{dz} = -\frac{1}{\sigma_{1,2}^2} \frac{d\Phi}{dz} \quad (3.1)$$

Subtracting Jeans equations for the two populations, we get

$$\frac{d \ln \frac{v_1 \sigma_1^2}{v_2 \sigma_2^2}}{dz} = -\left( \frac{1}{\sigma_1^2} - \frac{1}{\sigma_2^2} \right) \frac{d\Phi}{dz} \quad (3.2)$$

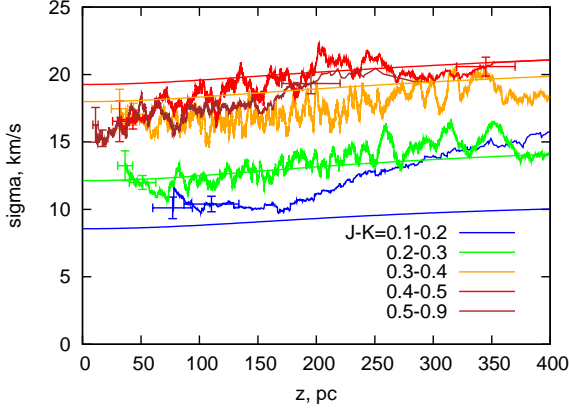


Figure 3.2: Velocity dispersion as function of height for different color bins. The height bin scans over  $z$ . The first point in the plot contains 100 stars, then the number of stars increases, and reaches 400 at the second point with error bars. Then it is 400 all the time up to the third point with error bars, after which the limiting condition is the width of the bin, which is not greater than 100 pc. The smooth lines are predictions of Just & Jahreißmodel.

This equation contains only the ratio of the two densities, thus can be used for samples with distance biases. The result of application of this equation to calculation of the surface density of the disc on different heights is plotted in Fig. 3.3.

### 3.3.4 Distribution over vertical energies

As far as selection function is different for different  $|z|$ , we introduce 10  $|z|$  bins and treat them separately. As far as a bin is narrow enough, we may assume that in each bin a fixed (though unknown) part of stars is observed. Then distribution of stars over energies must be the same for all the bins. Of course, not all the energies will be present in each  $|z|$  bin, the ones smaller than potential energy will be unattainable. It will change normalization of the observed part of the distribution  $f(E)$  and complicate putting together  $f(E)$  from different  $|z|$  bins. The borders of the bins are  $|z| = 60, 90, 120, 140, 160, 180, 210, 240, 280, 340, \text{ and } 400$  pc. Each bin is separated into  $|w|$  bins in such a way, that mean energy in each  $|z| - |w|$ -bin is one from the list 20, 60, 100, 140, 190, 250, 320, 410, 530, 700, 950, 1300 (km/s)<sup>2</sup>. Some of the bins are necessarily left empty. In such a way we get 10 curves  $f(E)$  for different  $|z|$  bins, that must be put together by vertical shifts, corresponding to unknown normalizations. We chose normalizations to minimize the expression

$$F = \sum_{a=1..N_z} \frac{\sum_{i=1..N_E, j=1..N_E} \frac{(f_{ai} - f_{aj})^2}{\Delta f_{ai}^2 \Delta f_{aj}^2}}{\sum_{i=1..N_E} \frac{1}{\Delta f_{ai}^2}}, \quad (3.3)$$

where  $f_{ai}$  is distribution function for  $i$ th value of energy in  $|z|$  bin  $a$ ,  $\Delta f_{ai}$  is its statistical error,  $N_z = 10$  is the number of  $|z|$  bins, and  $N_E = 12$  is the number of used mean values of  $E$ .

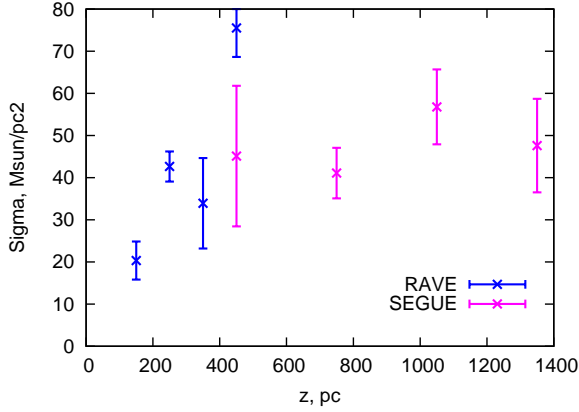


Figure 3.3: Estimates for the free fall acceleration as a function of height. The SEGUE sample is treated with Eq. 3.2, for the RAVE sample Kolmogorov-Smirnov test is used.

The allowed transformation is renormalization inside  $|z|$  bins,  $f_{ai} \rightarrow c_a f_{ai}$ , where  $c_a$  are some constants. If  $f_{ai}$  is not determined for some pairs of  $a$  and  $i$ , then we put corresponding  $\Delta f_{ai}$  to be infinity, and these bins fall out of the calculation. After the minimum of  $F$  is found we calculate the final distribution function as average throughout all the  $|z|$  bins:

$$f(E_i) = \frac{\sum_{i=1..N_E} \frac{f_{ai}}{\Delta f_{ai}}}{\sum_{i=1..N_E} \frac{1}{\Delta f_{ai}^2}}. \quad (3.4)$$

The overall normalisation is still free. Errors in the distribution function are found by variations. Each  $f_{ai}$  is varied by a random value which has normal distribution with dispersion  $\Delta f_{ai}$ , then the optimisation procedure is repeated, and new distribution function is found. By comparing the original distribution function with a set of perturbed ones, we find errors in the distribution function.

Distribution functions  $f(E)$  obtained for our 5 colour bins are plotted in Fig. 3.4-3.8. Overplotted are fittings by Sersic law

$$f(E) \propto \exp\left(-\left(\frac{E}{E_0}\right)^\alpha\right). \quad (3.5)$$

We see, that in all the cases de Vaucouleurs law gives a good approximation. But the inner maximum of velocity dispersion can't be reproduced by de Vaucouleurs law. It requires flattening of  $f(E)$  in the range  $E = 0..100$  (km/s)<sup>2</sup>.

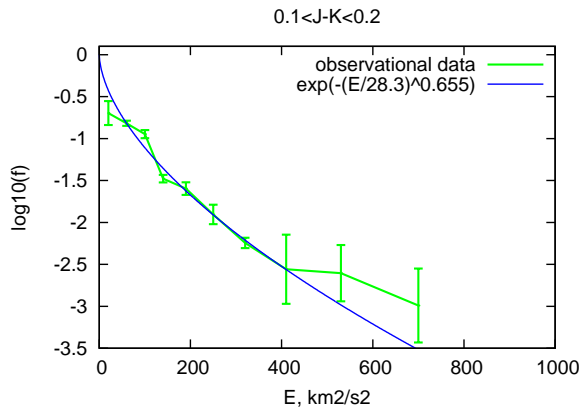


Figure 3.4: Distribution over vertical energies.

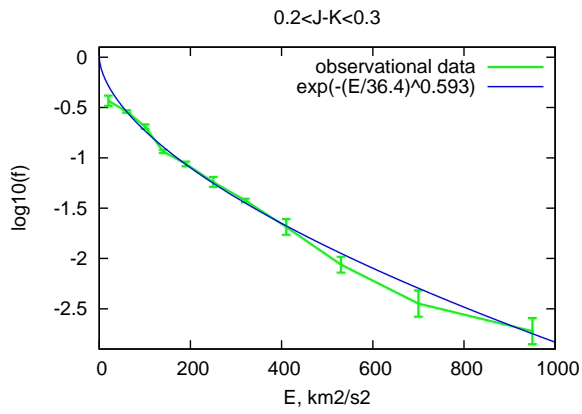


Figure 3.5: Distribution over vertical energies.

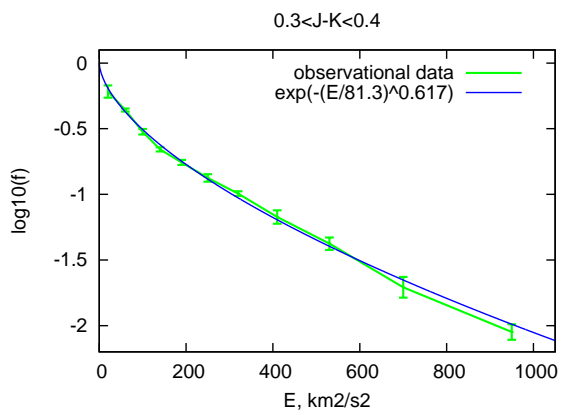


Figure 3.6: Distribution over vertical energies.

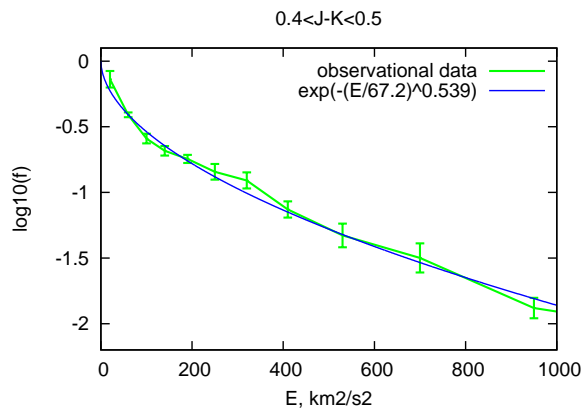


Figure 3.7: Distribution over vertical energies.

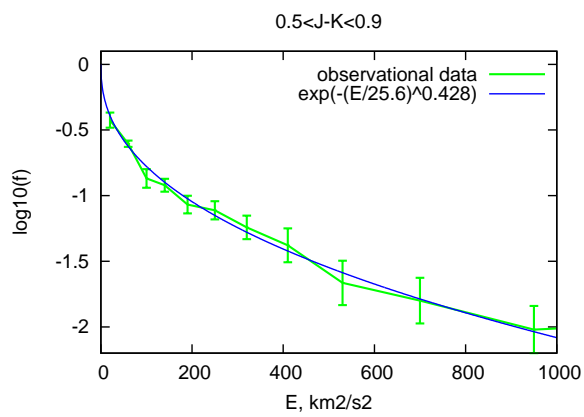


Figure 3.8: Distribution over vertical energies.



# 4

## Horizontal structure of the disc

### 4.1 Asymmetric drift and the local standard of rest

---

In this section asymmetric drift in the Galaxy is discussed. RAVE, SEGUE and Hipparcos data are used to measure it. RAVE provides the largest sample of dwarf stars and the application of the linear Strömberg relation leads to the tangential velocity of the Sun with respect to the local standard of rest  $V_{\odot} = 4.37 \pm 0.94 \text{ km s}^{-1}$ , consistent with the classical value based on Hipparcos data. Binning RAVE stars in metallicity reveals a bigger asymmetric drift corresponding to a smaller radial scalelength for more metal-rich populations, that is consistent with our expectations from the radial metallicity gradient in the disc. The content of this section was submitted to MNRAS (Golubov & Just (2012)).

#### 4.1.1 Introduction

To get the Galactic circular velocity from the observed mean rotation velocity of a sample, we must correct the mean velocity for the asymmetric drift. Moreover, asymmetric drift by itself provides an important probe of the Galaxy.

The asymmetric drift of a stellar population is defined as the difference between the velocity of a hypothetical set of stars possessing perfectly circular orbits, and the mean rotation velocity of the population under consideration. The velocity of the former is called the standard of rest. If the measurements are performed at the solar Galactocentric radius, it is the local standard of rest, or LSR. The determination of the LSR corresponds to measuring the peculiar motion ( $U_{\odot}, V_{\odot}, W_{\odot}$ ) of the Sun, where  $U_{\odot}$  is velocity of the Sun in the direction of the Galactic centre,  $V_{\odot}$  in the direction of the Galactic rotation, and  $W_{\odot}$  in the vertical direction. While measuring  $U_{\odot}$  and  $W_{\odot}$  is relatively straightforward,  $V_{\odot}$  requires a sophisticated asymmetric drift correction for its measurement, which is one goal of this paper.

Dehnen & Binney (1998) used a volume-complete sample of Hipparcos stars to constrain the LSR. They argued that the asymmetric drift  $V_a$  depends linearly on the squared radial velocity dispersion of a stellar population  $\sigma_R^2$ , extrapolated this linear dependence to zero velocity dispersion, and found the LSR. The velocity of the Sun in the direction of the Galactic rotation with respect to the LSR appeared to be  $V_{\odot} = 5.25 \pm 0.62 \text{ km s}^{-1}$ . Aumer & Binney (2009) applied a similar approach to the new reduction of the Hipparcos catalogue, and obtained the same value  $V_{\odot} = 5.25 \pm 0.54 \text{ km s}^{-1}$  but with a smaller error bar. The linear Strömberg relation

(Binney & Tremaine 2008) adopted in this analysis relies on the assumption that the structure (radial scale lengths and shape of the velocity dispersion ellipsoid) of the sub-populations with different velocity dispersion are similar. This assumption was discarded by Schönrich et al. (2010). Their chemodynamical model of a Milky Way like galaxy implied different radial scalelengths and different shapes of the velocity ellipsoid for different sub-populations, which resulted in a non-linear dependence  $V_a(\sigma_R^2)$ . Fitting the observed dependence  $V_a(\sigma_R^2)$  by predictions of their model, they got  $V_\odot = 12.24 \pm 0.47 \text{ km s}^{-1}$ , which is significantly larger than the classical value.

In this note we analyse the asymmetric drift and the LSR mainly based on the large and homogeneous sample of dwarf stars provided by an internal data set of the RAdial Velocity Experiment (RAVE, see Siebert et al. (2011) for the third data release) and complement it with other data sets.

We assume the Galactocentric radius of the Sun to be  $R_0 = 8 \text{ kpc}$ , which is consistent with most observational data up to date (Reid 1993; Gillessen et al. 2009). Assuming Sgr A\* to reside at the centre of the Galaxy and taking  $\mu_{1,A^*} = 6.37 \pm 0.02 \text{ mas yr}^{-1}$  for its proper motion in the Galactic plane (Reid & Brunthaler 2005), we find the rotation velocity of the Sun to be  $v_\odot = 241.6 \text{ km s}^{-1}$  in a Galactocentric coordinate system. This velocity consists of the circular velocity in the solar neighbourhood  $v_c$  (of the LSR) and the peculiar velocity of the Sun with respect to the LSR  $V_\odot$ , so that  $v_\odot = v_c + V_\odot$ . For the radial and vertical components of the LSR we assume  $U_\odot = 9.96 \text{ km s}^{-1}$  and  $W_\odot = 7.07 \text{ km s}^{-1}$  from Aumer & Binney (2009).

Even though most stars in our samples are relatively local, we make all computations in Galactocentric cylindrical coordinates. That is why we need  $R_0$  and  $\mu_{1,A^*}$  for our computations: they influence how velocities of distant stars are decomposed into radial and rotational components.

#### 4.1.2 The velocity ellipsoid

In order to take full advantage of the stellar parameter estimation in RAVE we split the sample into three metallicity bins with comparable sample sizes. We use these RAVE data sample to measure the shape and the orientation of the velocity ellipsoid.

The top panel of Figure 4.1 shows the radial velocity dispersion as a function of  $J - K$  colour. A clear trend with metallicity can be observed in the sense that lower metallicity shows larger velocity dispersion, which is only partly due to the bluer intrinsic colour.

The other panels of Figure 4.1 show the axis ratios of the velocity ellipsoid and the vertex deviation  $\alpha$  in the Galactic plane. The second panel shows the squared ratio of the velocity dispersions in the rotational and radial directions,  $\sigma_\phi^2/\sigma_R^2$ . There is a trend with velocity dispersion (which is discussed more in Sect. 5) but no significant differences for different metallicities. In the epicyclic approximation the ratio is connected to the local rotation curve by  $\sigma_\phi^2/\sigma_R^2 = \kappa^2/4\Omega^2 \sim 0.46$  for standard values (Binney & Tremaine 2008), where  $\kappa$  is the epicyclic frequency in the solar neighbourhood and  $\Omega$  is the orbital frequency. The observed deviations may be due to spiral structure at the low velocity dispersion end and due to non-linear effects at the high velocity dispersion end. The third panel demonstrates the ratio  $\sigma_z^2/\sigma_R^2$ . We can see that the ratio is bigger for bigger velocity dispersions and for lower metallicities.

In the bottom panel the vertex deviation  $\alpha$  of the velocity ellipsoid is plotted.  $\alpha$  is defined as the angle between the maximal eigenvector of the velocity ellipsoid projection onto the Galactic plane, and the direction towards the Galactic centre. The trend with metallicity is not significant due to the large error bars.

The radial and vertical components of the LSR from the RAVE data are  $U_{\odot} = 8.74 \pm 0.13$  km s<sup>-1</sup> and  $W_{\odot} = 7.57 \pm 0.07$  km s<sup>-1</sup>. They are in reasonable agreement with  $U_{\odot} = 9.96 \pm 0.33$  km s<sup>-1</sup> and  $W_{\odot} = 7.07 \pm 0.34$  km s<sup>-1</sup> from Aumer & Binney (2009). The discrepancy of order of 1 km s<sup>-1</sup> doesn't make a big difference in computations of velocity dispersions, as it is only added to the velocity dispersion quadratically.

### 4.1.3 The asymmetric drift

The asymmetric drift is governed by the Jeans equation (Binney & Tremaine 2008),

$$v_c^2 = \bar{v}_\phi^2 + \sigma_\phi^2 - \sigma_R^2 - \frac{R}{\nu} \frac{\partial(\nu\sigma_R^2)}{\partial R} - R \frac{\partial(\bar{\nu}v_z)}{\partial z}, \quad (4.1)$$

with tracer density  $\nu$  and mean tangential velocity  $\bar{v}_\phi$ . Roughly speaking, it expresses dynamical equilibrium in an axi-symmetric system within a volume element in a cylindrical coordinate system. The left-hand side represents the gravitational force in the Galactic potential, the first term on the right-hand side represents the centrifugal force, and the rest of the terms represent dynamical pressure and shear forces acting on the surfaces of the volume. There are two crucial assumptions for the validity of Eqn. (4.1), namely the axi-symmetry of the Galactic gravitational potential and the dynamical equilibrium of the stellar population under consideration. The former assumption can be broken by a spiral density wave, while the latter can be violated for young populations, whose mean age is smaller than the epicyclic period.

For simplicity we assume a flat rotation curve in the solar neighbourhood,  $v_c(R) \approx \text{const.}$  Then the Jeans equation is also valid for a stellar sample extending over a range of Galactocentric radii.

Standard assumptions that allow us to simplify Eqn. (4.1) include an exponential disc  $\nu \propto \exp(-R/R_d)$ , with an exponential radial velocity dispersion profile  $\sigma_R \propto \exp(-R/R_\sigma)$  (with  $R_d$  and  $R_\sigma$  being radial exponential scalelengths for the density and the velocity dispersion), and an alignment of the principal axes of the velocity ellipsoid with the spherical coordinate axes (the latter is argued by Binney 2010). These assumptions transform Eqn. (4.1) into

$$v_c^2 = \bar{v}_\phi^2 + \sigma_\phi^2 + \sigma_z^2 + \sigma_R^2 \left( \frac{R}{R_d} + \frac{2R}{R_\sigma} - 2 \right). \quad (4.2)$$

It is convenient to rewrite this equation, substituting  $v_c = v_{\odot} - V_{\odot}$  and  $\bar{v}_\phi = v_{\odot} - \Delta V$ , where  $-\Delta V$  is the mean rotational velocity of a stellar sample determined with respect to the Sun. In this notation the asymmetric drift velocity is given by  $V_a = v_c - \bar{v}_\phi = \Delta V - V_{\odot}$ . If we also assume that the shape of the velocity ellipsoid is constant,  $\sigma_R^2 \propto \sigma_\phi^2 \propto \sigma_z^2$ , and neglect the quadratic terms  $\Delta V^2$  and  $V_{\odot}^2$ , assuming  $\Delta V \ll \sigma_R$  and  $V_{\odot} \ll \sigma_R$ , then Eqn. 4.2 at the solar

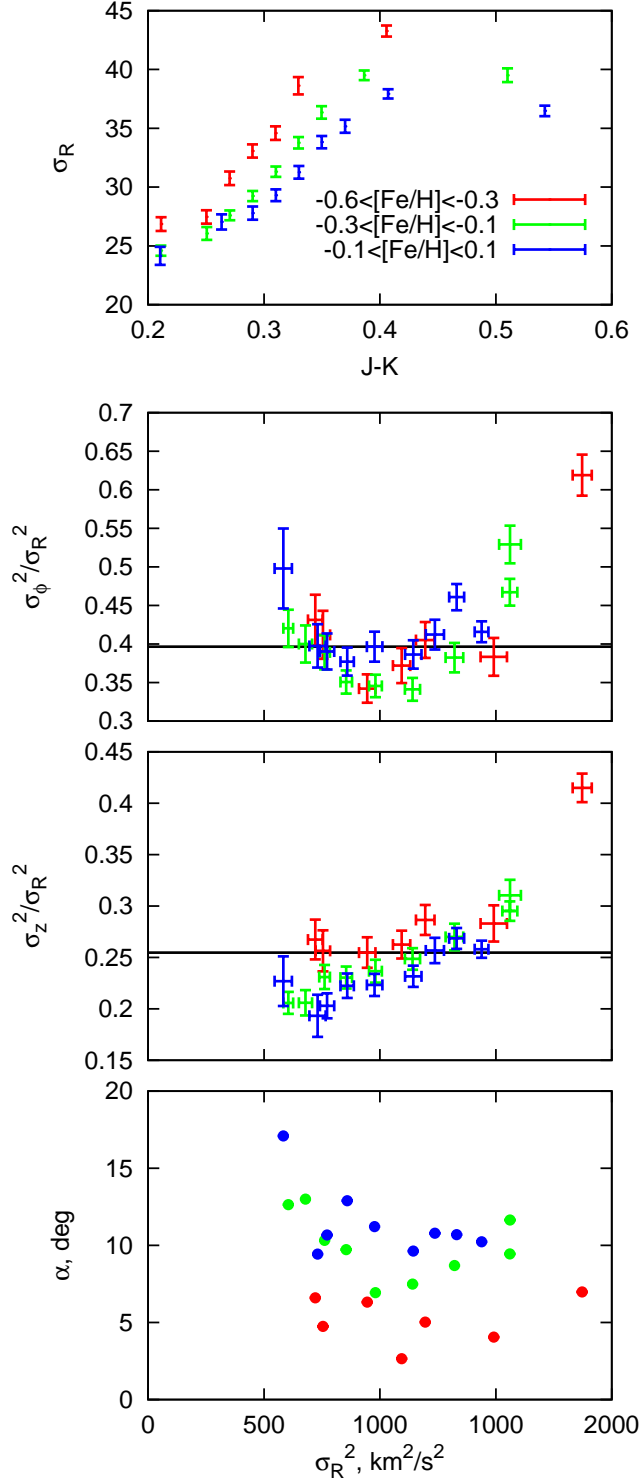


Figure 4.1: Properties of the velocity ellipsoid from the RAVE data. The upper panel shows the radial velocity dispersion as a function of colour. The second and the third panels present squared axis ratios of the velocity ellipsoid  $\sigma_\phi^2/\sigma_R^2$  and  $\sigma_z^2/\sigma_R^2$  as a functions of  $\sigma_R^2$  with the median values marked by horizontal lines. The bottom panel shows the vertex deviation  $\alpha$  of the velocity ellipsoid.

position  $R = R_0$  is transformed into the linear form of Strömberg's equation,

$$\begin{aligned} \Delta V &= V_\odot + K\sigma_R^2 \\ K &= \frac{1}{2v_\odot} \left( \frac{\sigma_\phi^2}{\sigma_R^2} + \frac{\sigma_z^2}{\sigma_R^2} - 2 + \frac{R_0}{R_d} + \frac{2R_0}{R_\sigma} \right), \end{aligned} \quad (4.3)$$

where  $K$  is a constant. If we assume additionally a constant thickness of the disc (which is ordinarily the case for external galaxies), then a constant shape of the velocity ellipsoid as a function of Galactocentric radius would imply  $v \propto \sigma_R^2$ , and therefore  $R_\sigma = 2R_d$ . This assumption together with estimates of the axis ratios of the velocity ellipsoid from Figure 4.1 allows us to transform Eqn. 4.3 into  $Kv_\odot = R_0/R_d - \text{const.}$ , and to use it to estimate  $R_d$  from the slope of the asymmetric drift curve.

Equation 4.3 predicts that  $\Delta V$  depends linearly on  $\sigma_R^2$ . We plot this dependence for our observational data in Figure 4.2, and for each bin plot its mean measured rotational velocity in terms of  $\Delta V$  versus its squared radial velocity dispersion  $\sigma_R^2$ .

We first discuss the RAVE data which show the smallest error bars. We see that the RAVE data can be fitted fairly well with a straight line (grey line in Figure 4.2). The best fitting value for the LSR is  $V_\odot = 4.37 \pm 0.94 \text{ km s}^{-1}$ , which is nicely consistent with  $V_\odot = 5.25 \pm 0.54 \text{ km s}^{-1}$  obtained by Aumer & Binney (2009) by a similar linear fit to Hipparcos data. The slope  $K = (90 \text{ km s}^{-1})^{-1}$  is also consistent with the classical value. An application of Eqn. 4.3 with the median ratios of the squared velocity dispersions ( $\sigma_\phi^2/\sigma_R^2 = 0.40$  and  $\sigma_z^2/\sigma_R^2 = 0.25$ , see Figure 4.1) results in a radial scale length of  $R_d = 2.27 \pm 0.12 \text{ kpc}$ .

SEGUE F and G dwarfs allow us to get only one significant point in the plot, and this point is consistent with the trend obtained from RAVE, while SEGUE M dwarfs seem to be off the trend. The local stars from the Hipparcos, the Catalogue of Nearby Stars (CNS4) and McCormick samples are also generally consistent with the best fitting line for RAVE, except for the two dynamically coldest bins – a feature, already observed by Dehnen & Binney (1998), which could be explained by the fact that the young stars have not yet reached dynamical equilibrium.

If the shape of the velocity ellipsoid and the scalelengths of the disc are different for different velocity dispersions, Eqn. 4.3 still can be applicable, but now  $K$  depends on the velocity dispersion  $\sigma_R$  of the sub-population. The chemodynamical model by Schönrich et al. (2010) probably can be interpreted in these terms. Each point of the non-linear dependence  $V_a(\sigma_R^2)$  from Schönrich et al. (2010) should correspond to Eqn. 4.3 with its own  $K$ . Thus observed or theoretically predicted asymmetric drift serves us as a measure of the bracket on the right-hand side of Eqn. 4.3. As terms with axis ratios of the velocity ellipsoid are less significant, the overall trend of  $K(\sigma_R^2)$  is dominated by the variations of the disc scalelengths  $R_d$  and  $R_\sigma$  with the velocity dispersions. Therefore the dependence  $V_a(\sigma_R^2)$  from Schönrich et al. (2010) can be interpreted as an increase of  $R_d$  and/or  $R_\sigma$  with the velocity dispersion  $\sigma_R$  of the sub-populations.

The increase of the observed  $V_a$  (or equivalently  $\Delta V$ ) in Figure 4.2 for the smallest velocity dispersions is inconsistent even with the model by Schönrich et al. (2010). A possible explanation is a spiral wave perturbation, which could influence the stellar dynamics in the

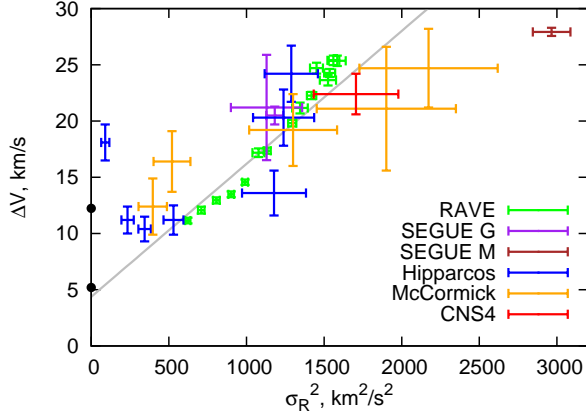


Figure 4.2: The asymmetric drift for different data sets. The two black circles on the  $\Delta V$  axis correspond to the different local standards of rest with  $V_{\odot} = 5.25 \text{ km s}^{-1}$  from Aumer & Binney (2009) and  $V_{\odot} = 12.24 \text{ km s}^{-1}$  from Schönrich et al. (2010), respectively. The grey line gives the best fit to the data points for RAVE dwarfs. It corresponds to the LSR  $V_{\odot} = 4.37 \text{ km s}^{-1}$  and the scalelength of the disc  $R_d = 2.27 \text{ kpc}$ .

solar neighbourhood. It would break the axi-symmetry of the gravitational potential implied by Eqn. 4.1, thus making all the further analysis inapplicable. The dynamically coldest sub-populations of stars are the most susceptible to small gravitational perturbations, while dynamically hotter sub-populations are much less affected by them. Thus a Jeans analysis could break down for small  $\sigma_R^2$ , while still being a good approximation for big  $\sigma_R^2$ . There is still no precise model to correct for these effects in the solar neighbourhood.

#### 4.1.4 Metallicity dependence

Binning stars of the RAVE sample in metallicities allows us to see more interesting features in the behaviour of the asymmetric drift. Even though the absolute calibration of the RAVE metallicity is not completely settled (Boeche et al. 2011), the metallicity  $[M/H]$  from the RAVE pipeline can be used as a relative indicator of the true metallicity. In Figure 4.3 we plot the mean rotational velocity in terms of  $\bar{v}_{\phi}$  versus its squared radial velocity  $\sigma_R^2$  for three different metallicity bins,  $-0.6 < [M/H] < -0.3$ ,  $-0.3 < [M/H] < -0.1$ , and  $-0.1 < [M/H] < 0.1$ . We see that stars at different metallicities demonstrate different asymmetric drifts, with more metal-poor stars having smaller asymmetric drifts and thus larger rotational velocities. This trend is consistent with the observed negative metallicity gradient in the Milky Way disc (e.g. as found by (Coşkunoğlu et al. 2012) also using RAVE dwarfs). Indeed, the inner parts of the Galaxy harbour more metal-rich stars than the outer parts. The higher fraction of metal-rich stars observed in the solar neighbourhood is expected to possess guiding radii smaller than  $R_0$ . It means that we are observing these stars closer to the apocentre of their orbits, that makes the observed mean rotational velocity smaller. In contrast, metal-poor stars are coming on

average from larger Galactocentric radii, resulting in a bigger mean rotational velocity. In terms of Eqn. (4.2) it means that metal-rich stars are more centrally concentrated, and have a smaller disc scale length  $R_d$ , while metal-poor stars have a bigger scale length  $R_d$ .

Since we have measurements of the shape of the velocity ellipsoid for each sub-sample, it is useful to separate observables and unknowns in the Jeans equation 4.1 by rewriting it into

$$\begin{aligned} V' &\equiv \Delta V - \frac{\sigma_\phi^2 + \sigma_z^2 - 2\sigma_R^2 + \Delta V^2}{2v_\odot} \\ &= V_\odot + \frac{\sigma_R^2}{2v_\odot} \left( \frac{R}{R_d} + \frac{2R}{R_\sigma} \right) - \frac{V_\odot^2}{2v_\odot}. \end{aligned} \quad (4.4)$$

leading at  $R_0$  to the linearized form

$$V' = V_\odot + K' \sigma_R^2, \quad \text{with} \quad K' = \frac{1}{2v_\odot} \left( \frac{R_0}{R_d} + \frac{2R_0}{R_\sigma} \right) \quad (4.5)$$

in linearized form. In this form we need to assume only equal radial scalelength for a linear fit to the data. In principle, this scalelength could be also a function of  $\sigma_R$ , thus implying a nonlinear dependence of  $K'$  in Eqn. (4.5). In some cases  $V_a$  can even become negative (Schönrich et al. 2010).

In Figure 4.3 the best joint linear fits to the data of the three metallicity bins based on Eqn. 4.3 (top panel) and on Eqn. 4.5 (bottom panel) are compared. We find for the LSR  $V_\odot = 4.59 \pm 1.00 \text{ km s}^{-1}$  ( $5.56 \pm 0.84 \text{ km s}^{-1}$  in the bottom panel), which is consistent with the estimate from Figure 4.2. The radial scalelengths of the disc are 1.94 (2.15 for the bottom panel), 2.42 (2.71) and 3.20 (3.69) kpc with decreasing metallicity. The systematically larger radial scalelengths in the bottom panel are mostly due to the shift of the LSR.

#### 4.1.5 Discussion

An extended, unbiased velocity catalogue of RAVE stars provides a very good tool to analyse stellar dynamics in the solar neighbourhood and to study the asymmetric drift. The observed dependence of the asymmetric drift velocity  $V_a$  on the squared radial velocity dispersion  $\sigma_R^2$  is linear with high accuracy, and linear extrapolation of this dependence to  $\sigma_R^2 = 0$  determines the LSR with  $V_\odot = 4.37 \pm 0.94 \text{ km s}^{-1}$ , which is consistent with the classical value (Aumer & Binney 2009). The trend of  $V_a(\sigma_R^2)$  from RAVE is also consistent with the asymmetric drift measured by means of other stellar samples, in particular Hipparcos and the SEGUE F- and G-dwarf sample.

A somewhat similar analysis of the RAVE data was performed by Coşkunoğlu et al. (2011). The authors used a kinematically selected sample of stars with photometric distances to determine the velocity of the Sun with respect to the neighbouring stars. We are using a bigger sample of stars, more reliable distances obtained from stellar models, and bin our stars independently of their velocities. The mean velocity of the Sun of about  $13 \text{ km s}^{-1}$  with respect to the local stars determined by Coşkunoğlu et al. (2011) is consistent with the mean  $\Delta V$  for the RAVE stars in Figure 4.2. Coşkunoğlu et al. (2011) did not to decompose this velocity

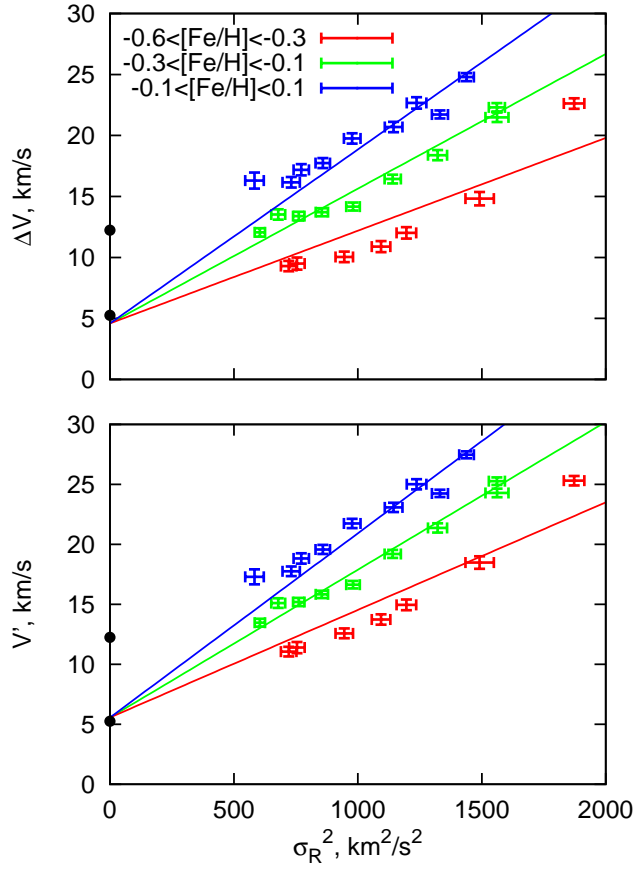


Figure 4.3: The asymmetric drift for the RAVE dwarfs separated into three metallicity bins:  $-0.6 < [\text{M}/\text{H}] < -0.3$ ,  $-0.3 < [\text{M}/\text{H}] < -0.1$ , and  $-0.1 < [\text{M}/\text{H}] < 0.1$ . The two black circles on the y-axis correspond to the LSR from Aumer & Binney (2009) and from Schönrich et al. (2010). The full lines show the best joint linear fit. Top: Using Eqn. (4.2). Bottom: Using Eqn. (4.5).

into velocity of the Sun with respect to the LSR and the velocity of the LSR with respect to the mean velocity of stars in their sample.

The measured LSR can be strongly affected by a spiral arm perturbation. Siebert et al. (2012) estimate variations of the mean  $v_\phi$  velocity to be of order of  $5 \text{ km s}^{-1}$  depending on the relative position of the observer with respect to the spiral arm. This contribution could be a possible reason for the non-linear dependence of  $V_a(\sigma_R^2)$  for small  $\sigma_R^2$ . Additionally the spiral arm perturbation could essentially influence the LSR computed with the aid of an equilibrium axi-symmetric model of the Galaxy.

From the slope of the asymmetric drift dependence on the radial velocity dispersion, we can estimate the radial scalelength of the Galactic disc. With the standard assumption  $R_\sigma = 2R_d$ , we get  $R_d = 2.3 \text{ kpc}$ . If  $R_\sigma$  is significantly larger than  $2R_d$ , as it is assumed by Bienaymé (1999), then  $R_d$  can be smaller than our estimate and even fall well below  $2 \text{ kpc}$ .

The observed dependence of the asymmetric drift on metallicity from RAVE data is consistent with our understanding of the metallicity distribution in the Milky Way disc. The best linear fit to the dependence gives a consistent value  $V_\odot = 4.59 \pm 1.00 \text{ km s}^{-1}$  for the LSR. The radial exponential scalelength of the disc is smaller for higher metallicities, implying a more centrally concentrated distribution of stars. The radial scalelength decreases from  $3.7 \text{ kpc}$  to  $2.2 \text{ kpc}$  for a metallicity increasing from  $[M/H] = -0.45 \text{ dex}$  to  $\pm 0 \text{ dex}$  in the disc computed from our data. The dependence of the asymmetric drift on metallicity can serve as a good constraint for chemodynamical models of the Milky Way and for the effect of radial migration on the stellar dynamics and abundance distribution in the solar neighbourhood.

## 4.2 Rotation curve of the Milky Way

Our aim is to construct a density model of the Milky Way, consistent with the observed rotation curve and with local density constraints. We reanalyze different sets of observational data for the rotation curve of the Milky Way. We calculate theoretical rotation curves for flattened density models, apply these flattened models for the Milky Way bulge and halo, and put them together with exponential disc to get density model of the Milky Way. When adjusting free parameters of the model to reproduce the observed rotation curve, we constrain ourselves with local matter and dark matter densities in the solar neighbourhood. We find that the best fit to the observations is given by a model consisting of flattened Hernquist bulge, exponential disc with a hole, and flattened cored isothermal dark matter halo. An outline of this chapter was published in Golubov et al. (2012).

### 4.2.1 Introduction

The rotation curve of the Milky Way provides important constraints on the density distribution in the Galaxy. Unfortunately, observation of rotation curve for the Milky Way is by far less straightforward than for external galaxies, and entails large errors, especially outside the solar radius. Nevertheless, we already have enough observations to constrain density distribution in the Galaxy fairly well.

Besançon model (Robin et al., Robin et al. (2003)) is probably the most successful achievement of this sort. Authors of the model combine Hipparcos results and the observed rotation curve to propose a self-consistent density model of the Milky Way.

A more recent density model derived from the rotation curve is presented in Sofue et al. (Sofue et al. (2009)). The authors compile observational data from radial velocities of HII regions, HI-disc thickness method, optical measurements of C stars, and VLBI observations to construct a synthetic rotation curve. The diverse data were re-calculated adopting the same galactocentric distance of the Sun  $R_0 = 8.0$  kpc and its circular velocity  $V_0 = 200$  km/s. The data were fitted with theoretical rotation curve produced by 3 mass components: de Vaucouleurs bulge, a cored isothermal dark matter halo, and an exponential disc with two overdensity rings, which were necessary to reproduce the behaviour of the observed rotation curve with minima at 2 kpc and at 9 kpc. Physical motivation for these high overdensities is somewhat questionable, and the very existence of the dip in the rotation curve at 9 kpc is uncertain due to high errors in the outer rotation curve. Another problem of the density model by Sofue et al. (Sofue et al. (2009)) are too high local matter and dark matter densities in the solar neighbourhood. They are about 1.5 times higher than the amounts obtained from analysis of the vertical dynamics of stars in the solar cylinder (Just et al., Just & Jahreiß (2010))

In this section we re-analyse the available observational data for the rotation curve of the Milky way, supplement them with our constraints of the behaviour of the rotation curve from SEGUE and RAVE data, and propose a density model of the Milky Way consistent with the observed rotation curve and density constraints for the solar neighborhood. In Sect. ?? we discuss available observational constraints for the rotation curve, and as well construct our own rotation curve in the solar neighborhood from SEGUE data. In Sect. 4.3 we discuss our

choice of mass components of the Milky Way. In Sect. 4.4 we adjust free parameters of our mass model to fit the observed rotation curve and the local density constraints. We discuss our results in Sect. ??.

### 4.2.2 Local density constraints

When constructing the density model of the Milky Way to reproduce the rotation curve we must always keep in mind local density and dark matter density constraints produced by observations of vertical stellar dynamics in the solar cylinder.

For the surface density of the Milky Way disc  $\Sigma_{\text{disc}}$  Holmberg & Flynn (Holmberg & Flynn (2004)) propose the value  $\Sigma_{\text{disc}} = 56 \pm 6 M_{\odot}/\text{pc}^2$ , while Just & Jahreiß (Just & Jahreiß (2010)) for their best fit model get  $\Sigma_{\text{disc}} = 45.2 \pm 4 M_{\odot}/\text{pc}^2$ , while other their models spread in  $\Sigma_{\text{disc}}$  from 41.8 to 50.4  $M_{\odot}/\text{pc}^2$ . Both the works are based on the analysis of Hypparcos sample. They are consistent with earlier estimates  $\Sigma_{\text{disc}} = 48 \pm 8 M_{\odot}/\text{pc}^2$  (Kuijken & Gilmore Kuijken & Gilmore (1991)),  $\Sigma_{\text{disc}} = 52 \pm 13 M_{\odot}/\text{pc}^2$  (Flynn & Fuchs Flynn & Fuchs (1994)), and to the estimated surface density of visible matter  $\Sigma_{\text{disc}} = 53 M_{\odot}/\text{pc}^2$  Holmberg & Flynn (Holmberg & Flynn (2004)).

The local density of DM halo in the solar neighbourhood is estimated in  $\rho_{h,0} = 0.014 M_{\odot}/\text{pc}^3$  by Just & Jahreiß (Just & Jahreiß (2010)) and in  $\rho_{h,0} = 0.0099 M_{\odot}/\text{pc}^3$  by Robin et al. (Robin et al. (2003)).

### 4.2.3 Local rotational velocity

The first point we can put on the rotation curve of the Milky Way is the point  $(R_0, V_0)$ , corresponding to the galactocentric distance and to rotational velocity of the local standard of rest. But even this point is subjected to essential uncertainties, producing uncertainties in other points whose derivation rely on an assumed local standard of rest  $(R_0, V_0)$  and solar velocity with respect to it  $(U_{\odot}, V_{\odot}, W_{\odot})$ .

Present amounts of  $U_{\odot}$  and  $W_{\odot}$  obtained from Hypparcos data seem to be reliable. The recent results by Schönrich et al. (Schönrich et al. (2010))  $U_{\odot} = 11.1^{+0.69}_{-0.75}$  km/s,  $W_{\odot} = 7.25^{+0.37}_{-0.36}$  km/s confirmed earlier results by Dehnen & Binney Dehnen & Binney (1998), Binney (Binney (2010)) In contrast to these two components, the amount of  $V_{\odot}$  was recently revisited, and the amount  $V_{\odot} = 5.2 \pm 0.6$  km/s by Dehnen & Binney (Dehnen & Binney (1998)), which had been considered to be fiducial for a decade, was risen to 11 km/s (Binney, Binney (2010)). Schönrich et al. (Schönrich et al. (2010)) get  $V_{\odot} = 12.24 \pm 0.47$  km/s, confirming these recent results.

Studies of Sgr A\* provide the most direct way to determine  $R_0$  and  $V_0$ . Reid & Brunthaler (Reid & Brunthaler (2005)) find proper motion to be  $\mu_{A^*} = 6.37 \pm 0.02$  mas/yr, that implies  $(V_0 + V_{\odot} + V_{S_{grA^*}})/R_0 = (30.2/pm0.1)$  km/s/kpc, where  $V_{S_{grA^*}}$  is an unknown peculiar velocity of Sgr A\* that probably is not greater than a few km/s. Usually  $V_{S_{grA^*}}$  is assumed to be 0, and we find a very precise estimate for the ratio of  $V_0$  to  $R_0$ . The amounts  $R_0 = 8$  kpc and  $V_0 = 200$  km/s recommended by IAU give  $(V_0 + V_{\odot})/R_0 = 26.5$  km/s/kpcare, that is completely inconsistent with the observatons.

Disentangling  $R_0$  and  $V_0$  is less straightforward and subjected to big errors. In his comprehensive review Reid (Reid (1993)) combined different estimates of distance to the Galactic centre, came out with the synthetic result  $R_0 = 8 \pm 0.5$  kpc and prognosed that we would know  $R_0$  with the accuracy of 3% till the year of 2000. Regretfully enough, we still haven't reached this limit, and Reid's paper still well presents our knowledge of  $R_0$ . More recent observations are also consistent with  $R_0 = 8$  kpc and still retain significant errors. Gillessen et al. (Gillessen et al. (2009)) get an estimate  $R_0 = 8.28 \pm 0.15|_{\text{stat}} \pm 0.29|_{\text{sys}}$  kpc from fitting orbit of S2 star in the Galactic centre. From VLBI observations with VERA Reid et al. (Reid et al. (2009)) find consistent values  $R_0 = 8.4 \pm 0.6$  kpc and  $V_0 = 254 \pm 16$  km/s.

In this section we adopt the local standard of rest from Schönrich et al. (Schönrich et al. (2010)), IAU recommended value  $R_0 = 8$  kpc that is consistent with all the available observations, and  $V_0 = 230$  km/s to get the correct proper motion of Sgr A\* by Reid & Brunthaler (Reid & Brunthaler (2005)).

#### 4.2.4 Tracing the rotation curve with SEGUE and RAVE stars

We consider several SEGUE samples to get rotation curve in the extended solar neighborhood. Properties and origins of these samples are listed in Table 4.1.

We plot average rotational velocities  $\bar{v}_\phi$  in bins with thin lines in Fig. 4.4. To transform  $\bar{v}_\phi$  into rotational velocity  $v_c$  we must correct for asymmetric drift.

By considering  $\phi$  component of Jeans equation, asymmetric drift correction can be proved to be given by formula (Binney & Tremaine Binney & Tremaine (2008)),

$$v_c^2 = \bar{v}_\phi^2 + \sigma_\phi^2 - \sigma_R^2 - \frac{R}{v} \frac{\partial(v\sigma_R^2)}{\partial R} - R \frac{\partial(\overline{v_R v_z})}{\partial z} \quad (4.6)$$

Now, following Binney & Tremaine (Binney & Tremaine (2008)), we do three simplifying assumptions.

Firstly, we assume the disc to be exponential. This assumption is consistent with observational data for the Milky Way and as well finds a strong confirmation in observations of external galaxies. But scale length of the disc  $R_d$  is still poorly constrained. To the best extent of our knowledge, we assume  $R_d=3.5$  kpc for the thin disc and  $R_d=2.5$  kpc for the thick disc.

Secondly, we assume that  $\sigma_R^2 \propto v$ . Assuming constancy of shape of velocity ellipsoid, this proportionality implies constancy of thickness of the disc.

Thirdly, we assume that principal axes of velocity ellipsoid retain alignment with the coordinate directions of spherical coordinates. Then

$$\overline{v_R v_z} \approx (\sigma_R^2 - \sigma_z^2)(z/R) \quad (4.7)$$

After applying these 3 assumptions to Eqn. 4.6, it turns into the following expression,

$$v_c^2 = \bar{v}_\phi^2 + \sigma_\phi^2 + \frac{2R}{R_d} \sigma_R^2 + \sigma_z^2 \quad (4.8)$$

Plot of circular velocity  $V_c$  is presented in Fig. 4.4.

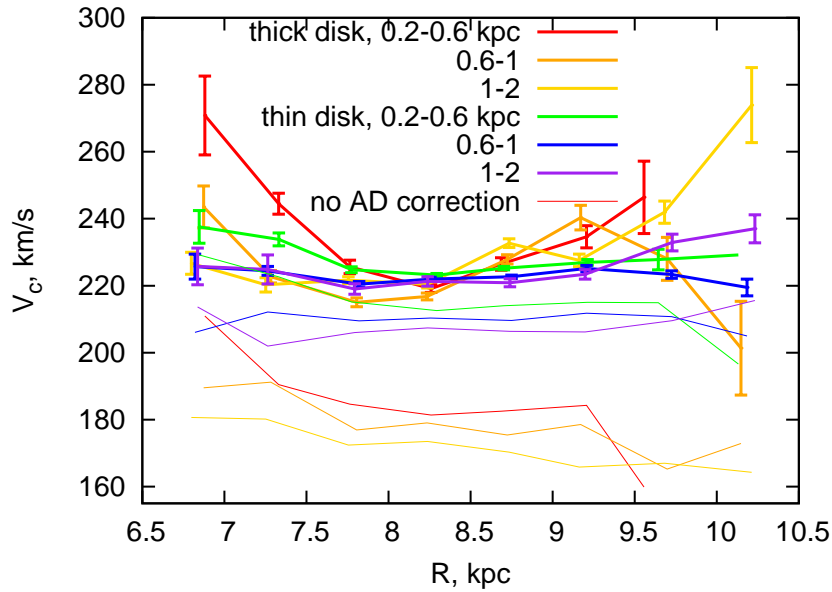


Figure 4.4: Rotation curve.

#### 4.2.5 Power index of the rotation curve

Another way of determining steepness of the rotation curve in the solar neighborhood is measuring the ratio of mean square deviation of  $v_\phi$  from circular rotational speed  $v_c$  to radial velocity dispersion  $\sigma_R$ . From epicyclic theory (Binney & Tremaine, Binney & Tremaine (2008)) this ratio is known to be

$$\frac{\overline{(v_\phi - v_c)^2}}{\sigma_R^2} = \frac{R}{2\Omega} \frac{\partial \Omega}{\partial R} + 1 \quad (4.9)$$

Let's assume power index of the rotation curve to be  $\alpha$ , so that  $V \propto R^\alpha$  and  $\Omega \propto R^{\alpha-1}$ . Then Eqn. 4.9 transforms into

$$\frac{\overline{(v_\phi - v_c)^2}}{\sigma_R^2} = \frac{\alpha + 1}{2} \quad (4.10)$$

Power indices  $\alpha$  resulting from velocity dispersions of our SEGUE and RAVE samples are given in the last column of Table 4.1.

This method doesn't need stellar samples covering the extended solar neighbourhood and can be equally well used for local stellar samples such as Geneva-Copenhagen survey (Holmberg et al. (Holmberg et al. (2009))), and this result is also included in Table 4.1. We can compare our result to the one presented in (Nordström et al. (Nordström et al. (2004))). The authors compare the ratio  $\sigma_V/\sigma_U$ , find the result 0.63, that is essentially different from 0.5, and conclude that the epicyclic theory with a flat rotation curve fails to explain the observed velocity dispersions. But if we compare this expression to Eqn. 4.1 we find two essential differences. Firstly, the ratio of velocity dispersions must be squared, secondly, the dispersion

Table 4.1: Properties of samples used for our analysis.

Description	Source	N stars	$\alpha$
G dwarfs, thin disc	Lee et al. (Lee et al. (2011))		$-0.04 \pm 0.02$
G dwarfs, thick disc	Lee et al. (Lee et al. (2011))		$0.04 \pm 0.02$
M dwarfs	West et al. (West et al. (2011))		$0.19 \pm 0.01$
GCS	Holmberg et al. (Holmberg et al. (2009))		$-0.02 \pm 0.01$

of  $\sigma_V$  must be calculated not with respect to its mean value, but with respect to rotational velocity, which can be essentially different due to asymmetric drift. And the resulting  $\alpha$  appears to be indistinguishable from 0.

Table 4.1 seems to rule out the fast decline of the rotation curve in the solar neighborhood with  $\alpha = -0.25$  predicted by Sofue et al. (Sofue et al. (2009)).

### 4.3 Rotation curves for 3-component density models

We use  $V_c$  for the circular speed in the Galactic plane ( $z = 0$ ). Dependence  $V_c(R)$  gives the rotation curve.  $V_c$  can be obtained by equating centripetal acceleration of the star to sum of gravitational accelerations produced by all the density components,

$$\begin{aligned} V_c^2 &= R \frac{d\Phi}{dR} = R \left( \frac{d\Phi_b}{dR} + \frac{d\Phi_d}{dR} + \frac{d\Phi_h}{dR} \right) = \\ &= V_{c,b}^2 + V_{c,d}^2 + V_{c,h}^2. \end{aligned} \quad (4.11)$$

Here  $\Phi_b$  stands for gravitational potential of bulge,  $\Phi_d$  for potential of disc, and  $\Phi_h$  for potential of halo.  $V_{c,b}$ ,  $V_{c,d}$  and  $V_{c,h}$  are circular velocities, which would be created by each density component alone. Contributions of bulge, disc and halo add up quadratically, as centripetal acceleration is proportional to velocity squared.

For a spherical mass distributions with enclosed mass  $M_r$  Eqn. 4.11 transforms into

$$V_c^2 = \frac{GM_r}{R} = (207\text{km/s})^2 \frac{M_r}{10^{10}M_\odot} \left( \frac{R}{\text{kpc}} \right)^{-1}. \quad (4.12)$$

An equation of the same form as 4.12 can also be applied for each component. Assuming that  $V_c$  isn't very different from 207 km/s (at least between 1 and 15 kpc) we get a famous rule of thumb for enclosed mass  $M_r \approx 10^{10} M_\odot \frac{R}{\text{kpc}}$ .

Spherical mass distributions for bulge and halo, though are simple and widely used models, are unrealistic. From observations of the Milky Way bulge and bulges of other galaxies we know that it must be flattened. Numerical simulations of dark matter accretion generally demonstrates formation of triaxial halos. Thus as a next step in the quest for realistic models we can consider a flattened mass distribution, where density depends on  $\sqrt{R^2 + z^2/q^2}$ , with  $R$  and  $z$  standing for cylindrical coordinates, and  $q$  for flattening.  $q = 1$  corresponds to spherical mass distribution, where density depends on spherical radius  $\sqrt{R^2 + z^2}$ .  $q < 1$  gives oblate,

and  $q > 1$  prolate density distributions. In many cases rotation curve of a flattened potential can be calculated analytically. The corresponding formulae are given in Table 2. The resulting formulae for rotation curves appear to be convenient for fitting observational data, though intricate and complex for comprehension.

Nevertheless, some consequences of flattening are intuitively evident. Flattened mass distributions lead to higher circular speed for the same enclosed mass (in ellipsoids or projected). As a consequence less enclosed mass is needed to reproduce the same rotation curve. A flattening of  $q = 0.5$  increases the circular speed (in the inner part) by about 10%,  $q < 0.1$  by 20% (see Fig. (2-12) for a modified Hubble profile and (2-17) for an exponential disc in Binney & Tremaine (Binney & Tremaine (2008)), hereafter BT). The radial shift of the maximum depends on the profile.

In this chapter we discuss  $V_c$  of different density components, their dependencies of density models, and the ways how the rotation curve can constrain the density model. The formulas for the flattened components are not reproduced here. Instead we give the simpler equations for spherical mass distributions, which are the limiting cases for  $q = 1$ .

### 4.3.1 Rotation curves for spherical density distributions

The generalised form of the NFW profile is

$$\rho(y) = \frac{\rho_0}{y^\beta(1+y)^{3-\beta}} \quad (4.13)$$

The parameters are connected to the cosmological quantities by (Navarro, Frank & White Navarro et al. (1996)) the virial radius  $r_{200}$ . This is the radius with mean density  $\bar{\rho}(r < r_{200}) = 200\rho_{crit}$  exceeding the critical density by a factor of 200. It can be written in the form

$$\begin{aligned} M_{200} &= M_r(r_{200}) = 200\rho_{crit} \frac{4\pi}{3} r_{200}^3 \\ \rho_{crit} &= \frac{3H_0^2}{8\pi G} \end{aligned} \quad (4.14)$$

The central density and the characteristic radius are quantified by two parameters

$$\begin{aligned} c &= y_{200} = \frac{r_{200}}{a} \\ \delta_c &= \frac{\rho_0}{\rho_{crit}} \end{aligned} \quad (4.15)$$

The standard model with  $\beta = 1$  can be integrated analytically.

In the literature two other modifications with core are discussed: the modified Hubble and the Burkert profiles with similar asymptotic behaviour.

Table 4.2: Rotation curves for different spherical density distributions. The first column presents name of the model, the second presents density  $\rho$  as function of dimensionless radius  $y = \frac{R}{a}$ , the third column gives squared circular velocity in Galactic plane as function of  $y$ .

Model	$\rho$	$V_c^2$
Singular isothermal	$\frac{\rho_0}{y^2}$	$4\pi G\rho_0 q a^2 \frac{\arcsin(\sqrt{1-q^2})}{\sqrt{1-q^2}}$
Cored isothermal	$\frac{\rho_0}{1+y^2}$	$4\pi G\rho_0 a^2 \left[1 - \frac{\arctg y}{y}\right]$
Hernquist	$\frac{\rho_0}{y(1+y)^3}$	$4\pi G\rho_0 a^2 \left(\frac{\ln(1+y)}{y} - \frac{1}{1+y}\right)$
NFW	$\frac{\rho_0}{y(1+y)^2}$	$4\pi G\rho_0 a^2 \left(\frac{\ln(1+y)}{y} - \frac{2+3y}{2(1+y)^2}\right)$
Cored NFW	$\frac{\rho_0}{(1+m)^3}$	$4\pi G\rho_0 a^2 \left(\frac{\ln(1+y)}{y} - \frac{2+3y}{2(1+y)^2}\right)$
Jaffe	$\frac{\rho_0}{y^2(1+y)^2}$	$4\pi G\rho_0 a^2 \left[\frac{\ln(y+\sqrt{1+y^2})}{y} - \frac{1}{\sqrt{1+y^2}}\right]$
Modified Hubble	$\frac{\rho_0}{(1+y^2)^{3/2}}$	$4\pi G\rho_0 a^2 \left[\frac{\ln(y+\sqrt{1+y^2})}{y} - \frac{1}{\sqrt{1+y^2}}\right]$
Burkert	$\frac{\rho_0}{(1+y)(1+y^2)}$	$2\pi G\rho_0 a^2 \left[\frac{\ln((1+y)\sqrt{1+y^2})}{y} - \frac{\arctg y}{y}\right]$

### 4.3.2 Rotation curves for flattened potentials

The rotation curve of an oblate spheroidal mass distribution  $\rho(m)$  with  $m^2 = (R^2 + z^2/q^2)/a^2$  can be calculated (in most cases numerically) by (BT 2-91)

$$V_c^2 = 4\pi G a^2 \int_0^y \frac{q\rho(y')y'^2 dy'}{\sqrt{y^2 - (1-q^2)y'^2}} \quad (4.16)$$

where

$$y' \equiv m(R', z=0) = \frac{R'}{a} \quad (4.17)$$

is distance normalized to a scale radius  $a$ . Here we used for  $z=0$  the integration variable  $R'$ . If we squeeze the spherical distribution by a factor  $q$ , we must rescale the density profile by a factor  $1/q$  in order to get the same enclosed mass (and total mass). For a set of profiles equation 4.16 can be integrated analytically by using the substitution

$$V_c^2 = 4\pi G a^2 \frac{q}{\sqrt{1-q^2}} \int_0^{x_m} y'^2 \rho(y') dx \quad (4.18)$$

where

$$y' = \frac{y \sin x}{\sqrt{1-q^2}} \quad (4.19)$$

$$\sin x_m = \sqrt{1-q^2} \quad (4.20)$$

Table 4.3: Rotation curves for different density distributions. The first column presents name of the model, the second presents density  $\rho$  as function of dimensionless radius  $m = \frac{1}{a} \sqrt{R^2 + \frac{z^2}{q^2}}$ , the third column gives squared circular velocity in Galactic plane as function of  $y = \frac{R}{a}$ .

Model	$\rho$	$V_c^2$
Singular isothermal	$\frac{\rho_0}{m^2}$	$4\pi G \rho_0 q a^2 \frac{\arcsin(\sqrt{1-q^2})}{\sqrt{1-q^2}}$
Cored isothermal	$\frac{\rho_0}{1+m^2}$	$4\pi G \rho_0 q a^2 \left[ \frac{1}{\sqrt{1-q^2}} \operatorname{arctg} \frac{\sqrt{1-q^2}}{q} - \frac{1}{\sqrt{1-q^2+y^2}} \operatorname{arctg} \frac{\sqrt{1-q^2+y^2}}{q} \right]$
Hernquist	$\frac{\rho_0}{m(1+m)^3}$	
NFW	$\frac{\rho_0}{m(1+m)^2}$	$\frac{4\pi G \rho_0 q a^2 y}{1-q^2-y^2} \left[ \frac{1-q+y}{1+y} - \frac{2y}{\sqrt{ y^2-(1-q^2) }} \operatorname{arctg} \frac{\sqrt{1-q^2-y^2}}{1+q+y} \right], y < \sqrt{1-q^2},$ $\frac{4\pi G \rho_0 q a^2 y}{1-q^2-y^2} \left[ \frac{1-q+y}{1+y} - \frac{2y}{\sqrt{ y^2-(1-q^2) }} \operatorname{artanh} \frac{\sqrt{y^2-(1-q^2)}}{1+q+y} \right], y > \sqrt{1-q^2}$
Jaffe	$\frac{\rho_0}{m^2(1+m)^2}$	$\frac{4\pi G \rho_0 q a^2}{y^2-(1-q^2)} \left[ \frac{y(1-q+y)}{(1+y)} - \frac{2(1-q^2)}{\sqrt{ y^2-(1-q^2) }} \operatorname{arctg} \frac{\sqrt{1-q^2-y^2}}{1+q+y} \right], y < \sqrt{1-q^2},$ $\frac{4\pi G \rho_0 q a^2}{y^2-(1-q^2)} \left[ \frac{y(1-q+y)}{(1+y)} + \frac{1-q^2}{\sqrt{ y^2-(1-q^2) }} \ln \left( \frac{y-\sqrt{y^2-(1-q^2)}}{y+\sqrt{y^2-(1-q^2)}} \frac{1-q+y+\sqrt{y^2-(1-q^2)}}{1-q+y-\sqrt{y^2-(1-q^2)}} \right) \right], y > \sqrt{1-q^2}$
Modified Hubble	$\frac{\rho_0}{(1+m^2)^{3/2}}$	$\frac{4\pi G \rho_0 q a^2 y}{\sqrt{1-q^2+y^2}} \left[ F \left( \arcsin \sqrt{\frac{1-q^2+y^2}{1+y^2}}, \frac{y}{\sqrt{1-q^2+y^2}} \right) - E \left( \arcsin \sqrt{\frac{1-q^2+y^2}{1+y^2}}, \frac{y}{\sqrt{1-q^2+y^2}} \right) \right]$

### 4.3.3 Bulge

**Dehnen models** We use mainly Dehnen (Dehnen (1993)) models for the bulge. In the spherical case we have

$$\rho(y) = \frac{\rho_0}{y^\gamma(1+y)^{4-\gamma}}, \quad (4.21)$$

$$M_r(y) = M_{\text{tot}} \left( \frac{y}{1+y} \right)^{3-\gamma}, \quad (4.22)$$

$$V_c^2(y) = \frac{GM_{\text{tot}}}{a} y^{2-\gamma} (1+y)^{\gamma-3}, \quad (4.23)$$

where  $y = r/a$  is dimensionless radius,  $M_r$  is enclosed mass, and  $\rho_0$  is central density,

$$\rho_0 = \frac{(3-\gamma)M_{\text{tot}}}{4\pi a^3} \quad (4.24)$$

The Hernquist model corresponds to  $\gamma = 1$  and the Jaffe model with isothermal cusp to  $\gamma = 2$ . For  $\gamma > 2$  the rotation curve is singular at the centre and for  $\gamma \geq 3$  the enclosed mass diverges. For  $\gamma > 2$  the rotation curve has maximum at  $y = 2 - \gamma$ . For reproducing the maximum of  $V_m = V_c(r_m)$  with different  $\gamma$ 's one needs to choose

$$a = r_m/(2-\gamma) \quad M_m = M_r(r_m) = \frac{r_m}{G} V_m^2 \quad (4.25)$$

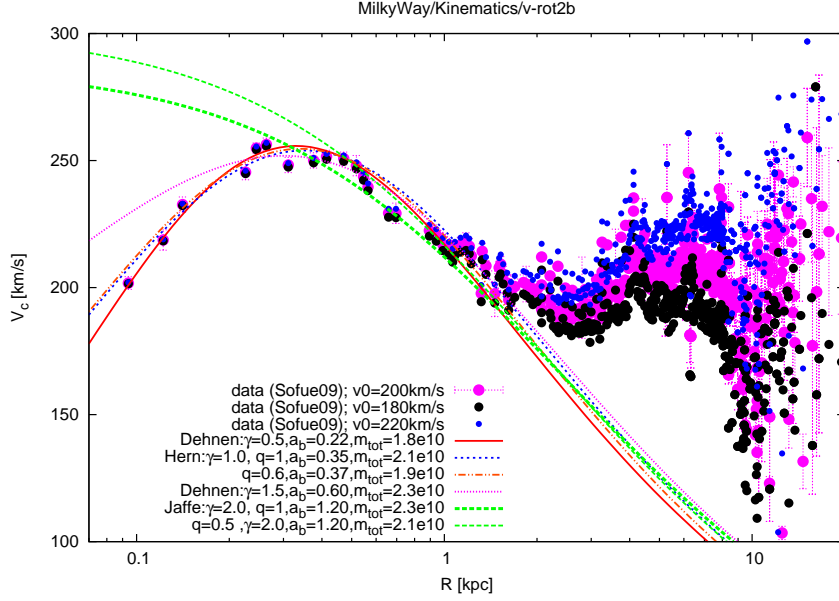


Figure 4.5: Data of Sofue et al. (Sofue et al. (2009)) with different  $V_0$  showing negligible influence inside  $R < 1$  kpc. Dehnen bulges with different cusp slopes  $\gamma$ , which match the maximum.

leading to

$$M_{\text{tot}} = M_m \left( \frac{3 - \gamma}{2 - \gamma} \right)^{3-\gamma} \quad (4.26)$$

For a Hernquist model the maximum is at  $r_m = a$  and the enclosed mass is  $M_{\text{tot}} = 4 M_m$ . For a shallow cusp with  $\gamma = 0.5$  we have  $M_{\text{tot}} = 3.59 M_m$  and for a steeper cusp with  $\gamma = 1.5$  we find  $M_{\text{tot}} = 5.2 M_m$ . Fig. 4.5 demonstrates Sofue et al. (Sofue et al. (2009)) inner rotation curve in logarithmic scale, thus best resolving the innermost kiloparsec of the Galaxy, where the bulge dominates. The uncertainty of the LSR makes us to use different  $V_0$  and to recalibrate the plots. The rotation curves for three different amounts of  $V_0$  are shown in Fig. 4.5 with different colours. We see that, in accordance with Eqn. 2.3, change of  $V_0$  makes almost no difference in the first kiloparsec, while for larger radii the spread in  $V_c$  is by far more essential.

The bulge is strongly flattened with  $q \approx 0.6$ , but we have no analytic formula for general  $\gamma$  values (only for Hernquist and Jaffe). The flattening leads to a reduced Bulge mass by about 10%.

We see that Jaffe model ( $\gamma = 2$ ) has uniformly decreasing  $V_c$ , and fails to reproduce maximum of  $V_c$  at 0.3 kpc. Dehnen model with  $\gamma = 1.5$  is also not steep enough in the first 0.2 kpc. The models with  $\gamma = 1$  (Hernquist) and  $\gamma = 0.5$  fit the data equally well. Total masses of the bulge for the best fit models are about  $2 \times 10^{10} M_\odot$ .

#### 4.3.4 Disc

The surface density for an exponential disc is given by

$$\Sigma(Y) = \Sigma_0 e^{-Y} = \Sigma_{sol} e^{Y_0 - Y}, \quad (4.27)$$

where  $Y = R/R_d$  is normalized radius,  $Y_0 = R_0/R_d$  is normalized radius of Sun, and  $R_d$  is scalelength of the disc,  $\Sigma_0$  is the surface density in the centre of the disc, and  $\Sigma_{sol}$  is the surface density of the disc at the solar radius  $R_0$ . The enclosed mass corresponding to the density from Eqn. 4.27 is

$$M_r(Y) = M_{tot} \left[ 1 - (1 + Y)e^{-Y} \right], \quad (4.28)$$

where the total disc mass  $M_{tot}$  is

$$M_{tot} = 2\pi\Sigma_0 R_d^2. \quad (4.29)$$

The rotation curve created by this mass distribution is given in terms of modified Bessel functions bY (BT 2-169)

$$V_c^2 = \frac{GM_{tot}}{R_d} \frac{Y^2}{2} [I_0(Y/2)K_0(Y/2) - I_1(Y/2)K_1(Y/2)] \quad (4.30)$$

In the Besançon model (Robin et al., Robin et al. (2003)) the authors claim that there is a hole in the exponential disc. For simplicity we model the hole by subtracting an exponential disc with a scale length smaller by a factor of  $n$  and a central surface density reduced by a factor of  $\epsilon$ .

The possible shapes of rotation curve caused by disc are presented in Fig. 4.6. For all the curves the local surface density is fixed at the level  $\Sigma_{sol} = 47M_\odot/\text{pc}^2$  in accordance to the local disc model by Just & Jahreiß (Just & Jahreiß (2010)). The disc scalelength is not that well constrained. We vary it in the range 2.5-4 kpc, and plot the results with the first four curves. The larger is the scalelength, the smaller is the density in the inner part of the Galaxy, and for the ranges of  $R$  and  $R_d$  under consideration, it causes a lower circular speed  $V_{rd}$ , and the four curves illustrate this trend. The next three curves illustrate discs with the same scalelength  $R_d = 2.8$  kpc, but with holes of different properties in the centre. The last curve examines the case when scalelengths of stellar and gas components of the disc are different. In accordance with Just & Jahreiß (Just & Jahreiß (2010)), we separate the local surface density  $47M_\odot/\text{pc}^2$  into  $34M_\odot/\text{pc}^2$  belonging to stellar component, and  $13M_\odot/\text{pc}^2$  belonging to gas. The scalelength of stellar component is again  $R_d = 2.8$  kpc, the scalelength of gas is assumed to be twice larger. The plot demonstrates that neither hole inside the disc nor different scalelength of gas change the rotation curve essentially, in contrast to scalelength  $R_d$ , to which the rotation curve is very sensitive.

Nevertheless, hole inside the disc appears to be important in reproducing the observed dip of the rotation curve at 2 kpc, as it is illustrated in Fig. 4.7. The plot demonstrates the sum of Hernquist bulge (the same as in Fig. 4.5) and a disc with different kinds of a hole, overplotted with the observational points from Sofue et al. Sofue et al. (2009) renormalized on  $V_0 = 220$  km/s. Three different values are chosen for the ratio of the disc and the hole scale radii  $n$ , and for each  $n$  two values of ratio of central densities  $\epsilon$  were used. The curve must fit the data

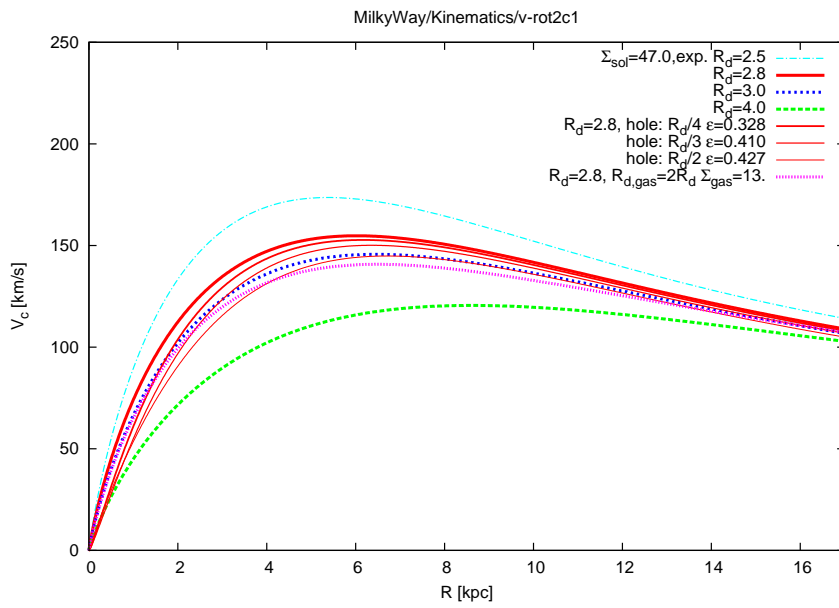


Figure 4.6: Exponential discs with fixed local surface density: variation of scale length and cutting out an inner hole by subtracting an exponential disc with reduced scale length  $R_d/n$  and reduced central surface density  $\epsilon$  (chosen to just avoid a negative  $V_c^2$  of the disc at the centre). The last (pink) line shows the effect of a gas disc with twice the scale length, where  $13M_\odot/pc^2$  of the local surface density of  $47M_\odot/pc^2$  is attributed to the gas disc.

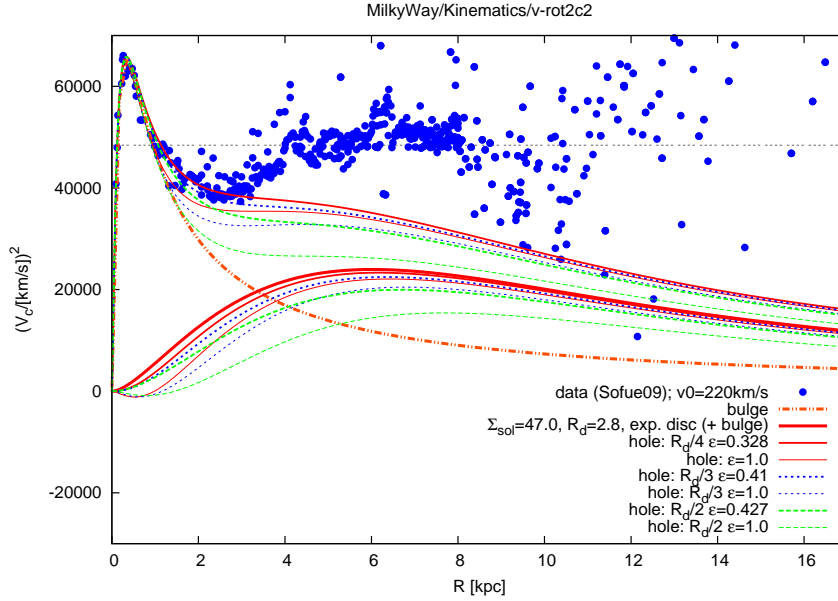


Figure 4.7: Plot of  $V_c^2$ , where the components add up linearly: Effect of a hole in the exponential disc with respect to reproduce the strong decline around  $R = 2$  kpc. The bulge is a Hernquist model with parameters as in figure 4.5 for  $\gamma = 1.0$ .

points after adding up the halo. We can already see that the lower and upper plots can barely reproduce the observations, and scale radius  $R_d/3$  seems to be the most favourable for the hole.

### 4.3.5 DM Halo

We compare two standard halo models, cored isothermal profile and Navarro-Frenk-White profile.

**Cored isothermal models** The spherical isothermal case with core is given by density distribution

$$\rho(y) = \frac{\rho_0}{1 + y^2}. \quad (4.31)$$

Circular velocity of the cored isothermal profile is

$$V_c^2(y) = 4\pi G \rho_0 a^2 \left[ 1 - \frac{\arctg y}{y} \right]. \quad (4.32)$$

Fixing the local density  $\rho_0 a^2 / (R_0^2 + a^2)$  means, that the circular velocity at infinity is proportional to  $\sqrt{R_0^2 + a^2}$ . The expected flattening is not too strong (at most  $q = 0.8$  for the density distribution). The corresponding flattening of the iso-potential surfaces is  $\sim 0.9$ .

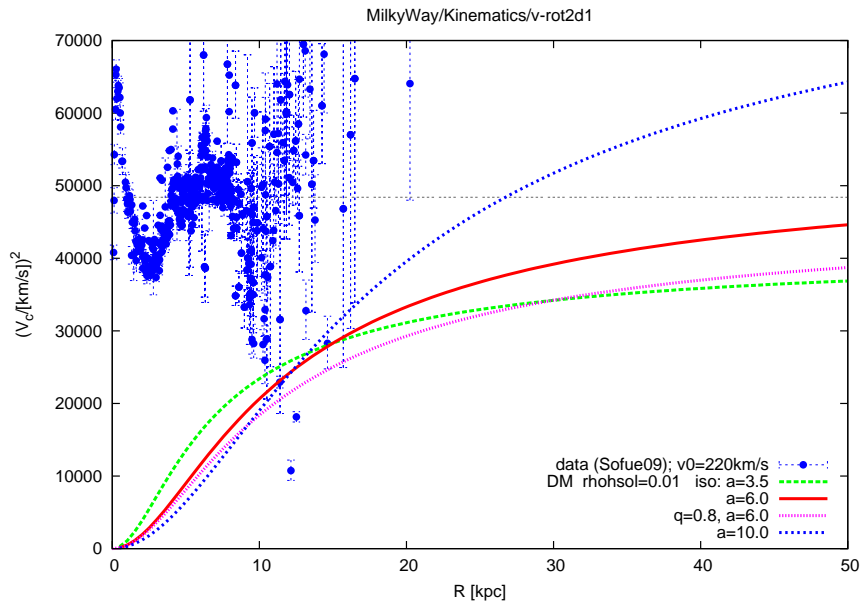


Figure 4.8: DM halo with local density fixed to  $\rho_{h,0} \approx 0.01 M_{\odot}/\text{pc}^3$ . Isothermal models with different core radius and the effect of flattening.

Rotation curves for cored isothermal halos are presented in Fig. 4.8. For all the curves local dark matter density is fixed to  $\rho_{hsol} = 0.01 M_{\odot}/\text{pc}^3$ , while scale radius  $a$  and flattening  $q$  are varied.

The main effect of fixing the local density  $\rho_0$  is that the cusp requires a large contribution to the inner rotation curve for all scale radii.

#### 4.4 Fitting observed rotation curve of the Milky Way with a density model

**Full models** A full 3 component model with Bulge, disc and DM halo, which fits the rotation curve and the local constraints, is shown in figure 4.12 adopting  $(R_0, V_0)=(8 \text{ kpc}, 220 \text{ km/s})$ . The isothermal halo fits better the local minimum at  $R = 2 - 3 \text{ kpc}$ . Up to 3 or 4 kpc bulge gives the main contribution to rotational velocity, around 5 kpc disc slightly overwhelms the other two component, and starting from about 7 kpc halo contribution dominates. At the solar radius the contribution of the DM halo is around 50%.

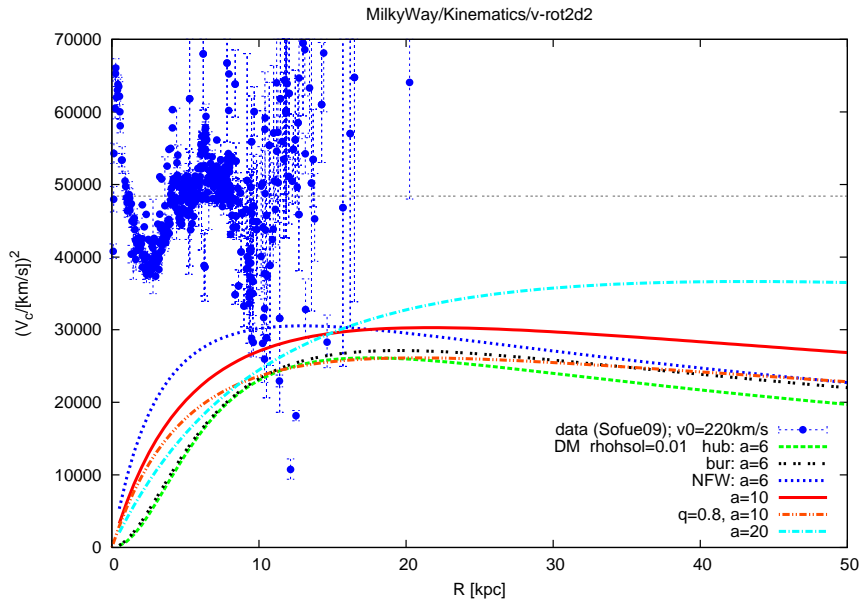


Figure 4.9: DM halo with local density fixed to  $\rho_{h,0} \approx 0.01 M_{\odot}/\text{pc}^3$ . NFW model with different scale radius and flattening. Additionally the modified Hubble and the Burkert models are shown.

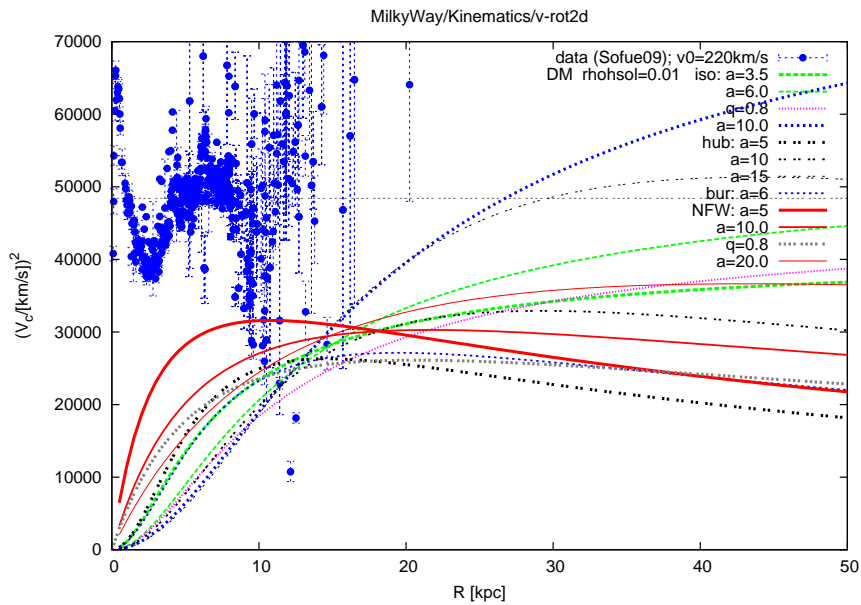


Figure 4.10: Plot of  $V_c^2$  for different DM halo models with fixed local volume density and varying scale radius.

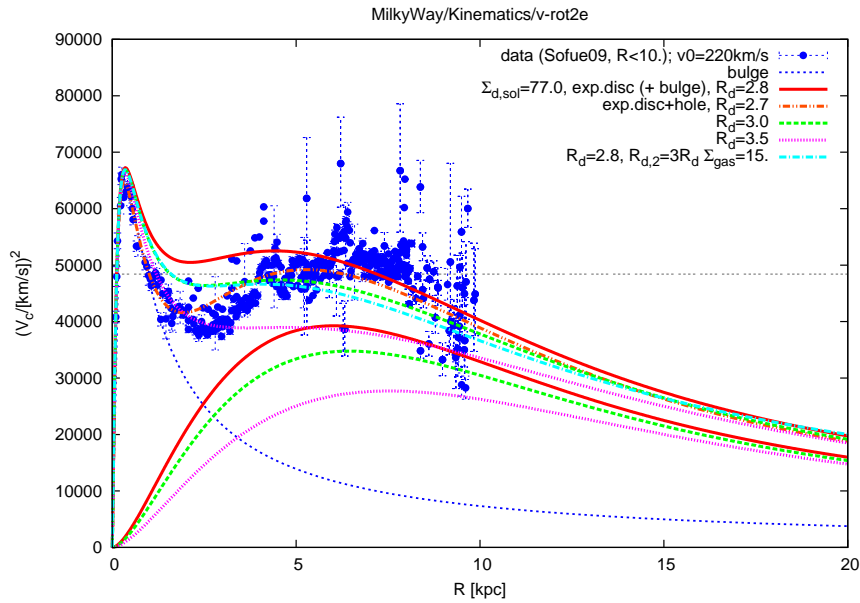


Figure 4.11: Plot of  $V_c^2$  for bulge + disc models (no DM halo) with maximum local surface density and varying scale length. The model with a hole ( $R_d/3$  and  $\epsilon = 0.8$ ) can in principle reproduce the inner rotation curve.

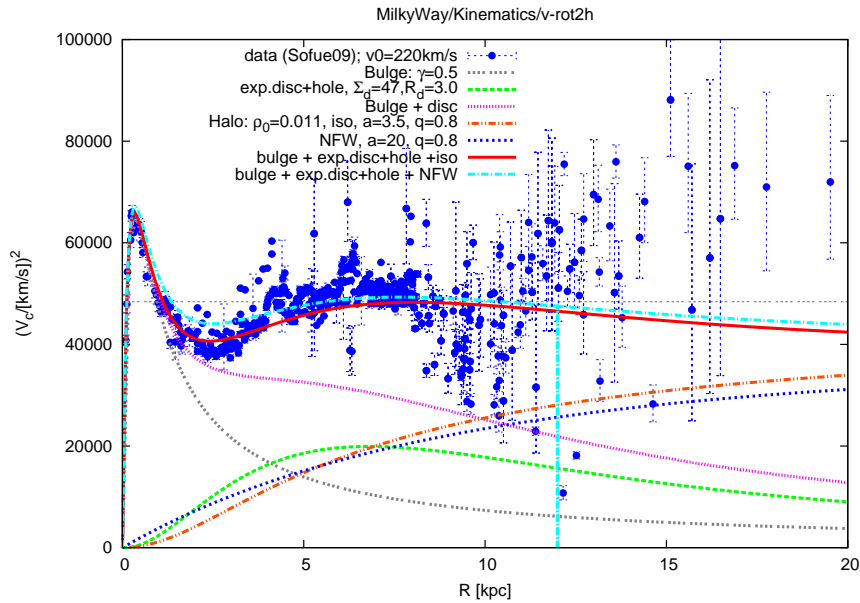


Figure 4.12: Plot of  $V_c^2$  for bulge + disc + halo models. The bulge is a Dehnen model with  $M_b = 1.8e10M_\odot$  and a scale radius of  $a_b = 0.22$  kpc. The disc is an exponential disc with  $R_d = 3.0$  kpc with a hole ( $R_d/3$  and  $\epsilon = 0.4$ ). The total disc mass is  $M_d = 4.3 \times 10^{10}M_\odot$ .

# 5

## Perspectives

### 5.1 Distribution functions in the plane of the Milky Way disc

---

We construct distribution functions of stars over the two components of the velocity in the plane of the Milky Way, and to compare them with the observations.

#### 5.1.1 Epicyclic approximation

Let's consider the simplest model of the Milky Way disc. We assume the rotation curve to be flat with the rotation velocity  $V_0$ , and use epicyclic approximation. Each star can be described by its guiding radius  $R_g$ , epicyclic velocity  $u$  (radial velocity when crossing the epicyclic radius), and epicyclic phase  $\phi$ . Then the observed rotational velocity  $V$ , radial velocity  $U$ , and galactocentric radius  $R$  of the star are

$$V = V_0 + \frac{u}{\sqrt{2}} \cos \phi, \quad (5.1)$$

$$U = -u \sin \phi, \quad (5.2)$$

$$R = R_g - \frac{u R_g}{\sqrt{2} V_0} \cos \phi. \quad (5.3)$$

We assume an exponential distribution over guiding radii, with the scale length  $R_\Sigma$  and the local surface density of guiding centres  $\Sigma_{g0}$  in the solar neighbourhood  $R_0$ ,

$$\Sigma_g(R) = \Sigma_{g0} e^{-\frac{R-R_0}{R_\Sigma}}. \quad (5.4)$$

Note, that the exponential scale length and the local surface density of guiding centres  $R_\Sigma$  and  $\Sigma_{g0}$  don't have to be equal to the exponential scale length and the local surface density of stars  $R_d$  and  $\Sigma_0$ , as the latter two are also affected by blurring due to epicyclic rotation. Distribution over epicyclic velocities is assumed to be two-dimensional Gaussian,

$$dN \propto \frac{u du}{\sigma^2} \exp\left(-\frac{u^2}{2\sigma^2}\right). \quad (5.5)$$

The dispersion  $\sigma$  is also assumed to depend on the radius exponentially,

$$\sigma(R) = \sigma_0 e^{-\frac{R-R_0}{R_\sigma}}. \quad (5.6)$$

All phases  $\phi$  are assumed to be equally probable. Then the number of stars with a given guiding radius, epicyclic velocity, and epicyclic phase, are

$$dN = 2\pi\Sigma_g R_g dR_g e^{-\frac{u^2}{2\sigma^2}} \frac{udu d\phi}{\sigma^2 2\pi} \quad (5.7)$$

Then we invert Eqs. 5.1, 5.2, 5.3, to express  $u$ ,  $\phi$ , and  $R_g$  in terms of  $U$ ,  $V$ , and  $R$ ,

$$u = \sqrt{U^2 + (V - V_0)^2}, \quad (5.8)$$

$$\phi = -\arctan \frac{U}{\sqrt{2}(V - V_0)}, \quad (5.9)$$

$$R_g = R + \frac{(V - V_0)R}{2V_0 - V}. \quad (5.10)$$

Now we use Eqs. 5.8, 5.9, 5.10, to transform Eq. 5.7 to variables  $U$ ,  $V$ , and  $R$ . When performing this transformation, we must mention that the Jacobian of the transformation is  $\frac{\partial(u,\phi,R_g)}{\partial(U,V,R)} = \sqrt{\frac{2}{U^2+2(V-V_0)^2}} \frac{V_0}{2V_0-V}$ . Then we make the substitution  $dN/(2\pi R dR) = d\Sigma$ , and thus get the following expression,

$$d\Sigma = \frac{\Sigma_{g0}}{\sqrt{2}\pi} \left( \frac{V_0}{2V_0 - V} \right)^2 e^{-\left(\frac{1}{R_\Sigma} - \frac{2}{R_\sigma}\right)\left(R - R_0 + \frac{(V-V_0)R}{2V_0-V}\right) - \frac{U^2+2(V-V_0)^2}{2\sigma_0^2}} e^{-\frac{2}{R_\sigma}\left(R - R_0 + \frac{(V-V_0)R}{2V_0-V}\right)} \frac{dU dV}{\sigma_0^2} \quad (5.11)$$

This equation presents the distribution of stars over the two components of the velocity.

### 5.1.2 Precise integration of orbits in 2D with a flat rotation curve

Let us now reject epicyclic approximation, and precisely integrate the orbit in 2 dimensions, still assuming the flat rotation curve. Then the effective potential for the radial motion of a star is

$$V_{eff} = V_0^2 \ln \frac{R}{R_g} + \frac{V_0^2 R_g^2}{2} \left( \frac{1}{R^2} - \frac{1}{R_g^2} \right). \quad (5.12)$$

It gives the following expression for epicyclic energy of the star,

$$\mathcal{E} = V_0^2 \ln \frac{R}{R_g} + \frac{V_0^2 R_g^2}{2} \left( \frac{1}{R^2} - \frac{1}{R_g^2} \right) + \frac{U^2}{2}. \quad (5.13)$$

We assume the surface density of guiding centres to have the same form of Eq. 5.4. The distribution over epicyclic energies is assumed to be exponential,

$$dN \propto \frac{d\mathcal{E}}{\sigma^2} \exp\left(-\frac{\mathcal{E}}{\sigma^2}\right). \quad (5.14)$$

This formula is a generalization of Eq. 5.5. The dispersion  $\sigma$  is assumed to be expressed by Eq. 5.6.

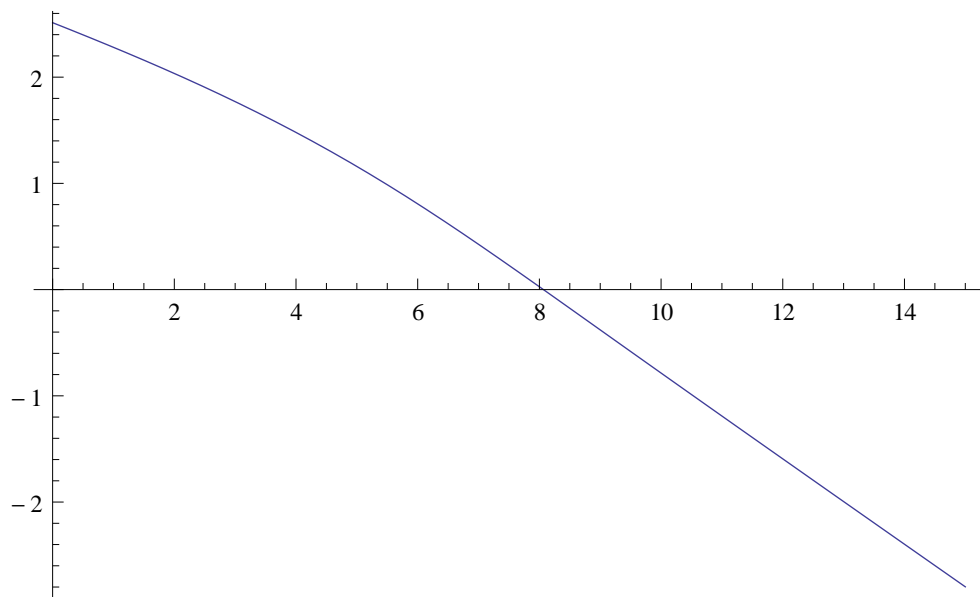


Figure 5.1: Theoretical disc surface density distribution in epicyclic approximation.  $R_{\Sigma} = 2.5$  kpc,  $R_{\sigma} = 5$  kpc,  $V_0 = 240$  km/s,  $R_0 = 8$  kpc,  $\sigma_0 = 38$  km/s.

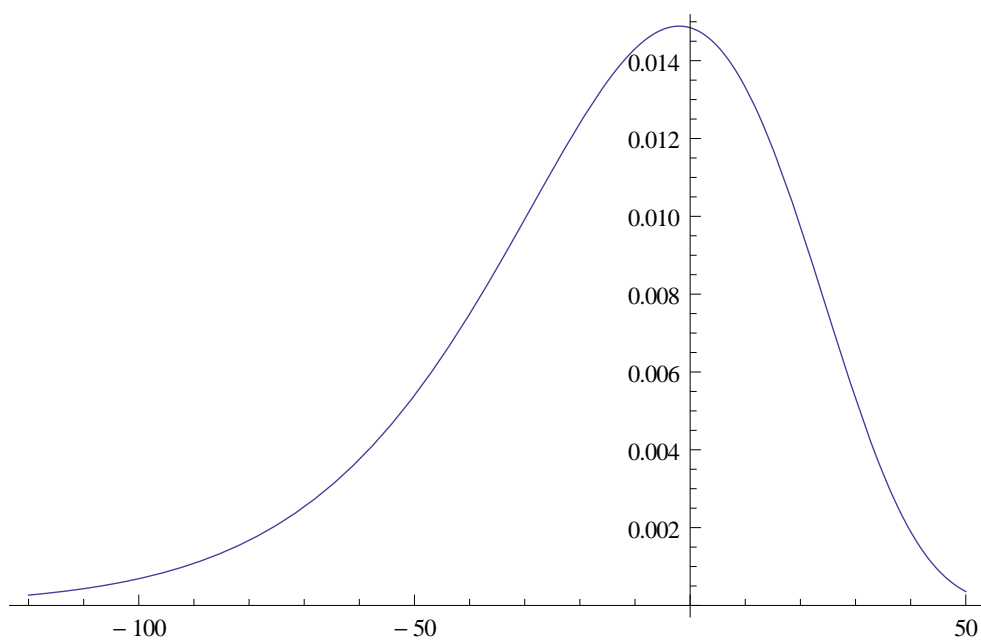


Figure 5.2: Theoretical distribution over velocities  $V$  in epicyclic approximation.  $R_{\Sigma} = 2.5$  kpc,  $R_{\sigma} = 5$  kpc,  $V_0 = 240$  km/s,  $R_0 = 8$  kpc,  $\sigma_0 = 38$  km/s.

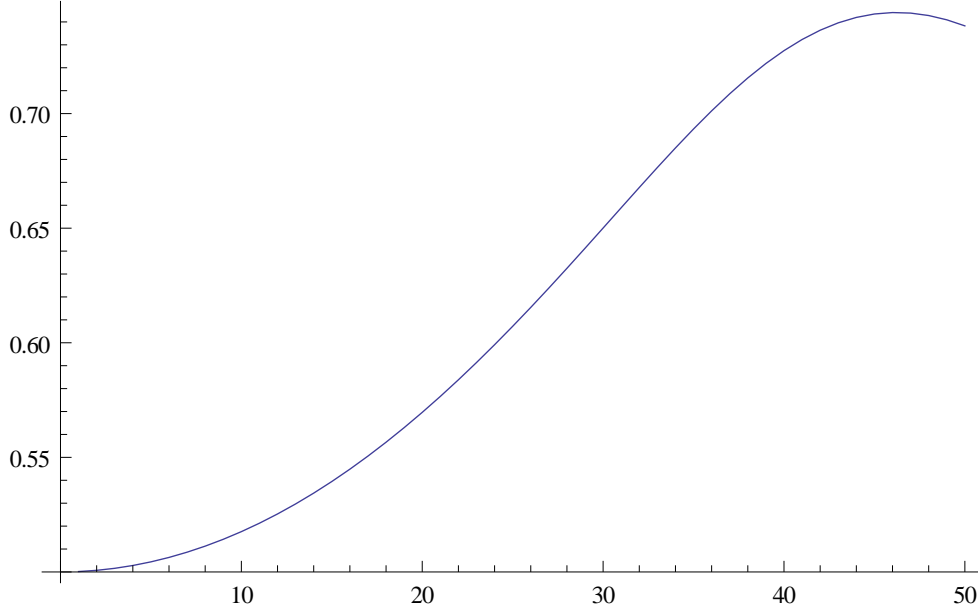


Figure 5.3: Theoretical ratio of rotational and radial velocity dispersions in epicyclic approximation.  $R_{\Sigma} = 2.5$  kpc,  $R_{\sigma} = 5$  kpc,  $V_0 = 240$  km/s,  $R_0 = 8$  kpc.

Then we can write the following expression for the number of stars with given guiding radius  $R_g$  and epicyclic energy  $\mathcal{E}$  observed at a given galactocentric radius  $R$ ,

$$dN = 2\pi R_g \Sigma_{g0} e^{-\frac{R_g - R_0}{R_{\Sigma}}} dR_g e^{-\frac{\mathcal{E}}{\sigma_0^2}} e^{-\frac{2(R_g - R_0)}{R_{\sigma}}} e^{-\frac{2(R_g - R_0)}{R_{\sigma}}} \frac{d\mathcal{E}}{\sigma_0^2} \frac{2dR}{T|U|} \quad (5.15)$$

The ultimate term gives the fraction of time, which is spent by a star between radii  $R$  and  $R + dR$ . Here  $U$  is the radial velocity of the star determined from Eq. 5.13,

$$U = \pm \sqrt{2\mathcal{E} - 2V_0^2 \ln \frac{R}{R_g} + V_0^2 R_g^2 \left( \frac{1}{R^2} - \frac{1}{R_g^2} \right)}. \quad (5.16)$$

$T$  is epicyclic period,

$$T = \int_{R_{min}}^{R_{max}} \frac{2dR}{\sqrt{2\mathcal{E} - 2V_0^2 \ln \frac{R}{R_g} + V_0^2 R_g^2 \left( \frac{1}{R^2} - \frac{1}{R_g^2} \right)}}. \quad (5.17)$$

With a reasonable precision  $T$  can be approximated as

$$T \approx \frac{\sqrt{2\pi} R_g}{V_0} e^{-\frac{\mathcal{E}}{V_0^2}} \quad (5.18)$$

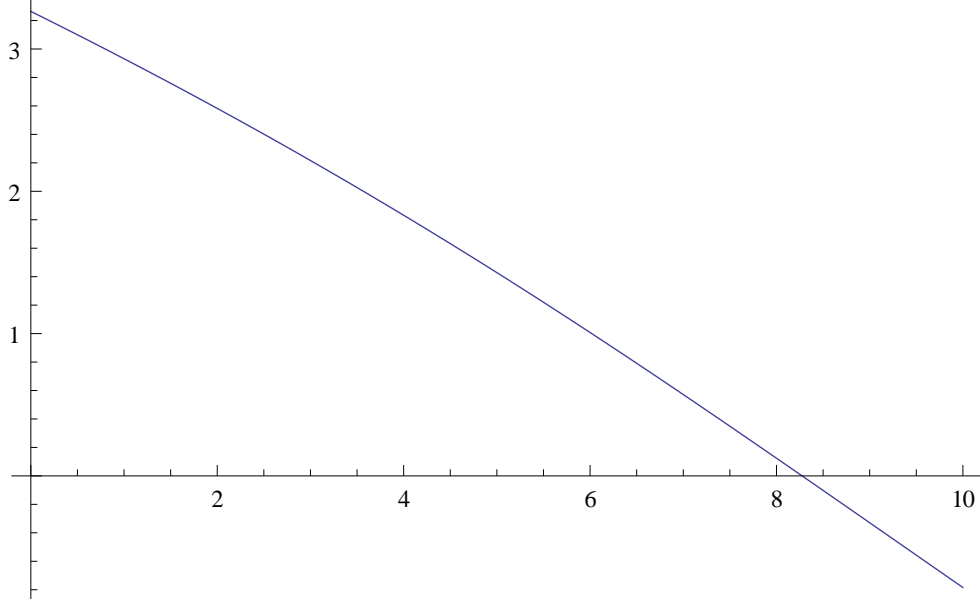


Figure 5.4: Theoretical disc surface density distribution for flat rotation curve.  $R_\Sigma = 2.3$  kpc,  $R_\sigma = 8$  kpc,  $V_0 = 240$  km/s,  $R_0 = 8$  kpc,  $\sigma_0 = 38$  km/s.

Equation 5.15 must be transformed to the variables  $U$ ,  $V$ , and  $R$ . The Jacobian of the transformation is  $\frac{\partial(\mathcal{E}, R_g, R)}{\partial(U, V, R)} = \frac{UR}{V_0}$ . Thus we get

$$d\Sigma = \frac{\Sigma g_0}{\sqrt{2\pi}} e^{-\left(\frac{1}{R_\Sigma} - \frac{2}{R_\sigma}\right)\left(R - R_0 + \frac{(V - V_0)R}{V_0}\right) - \frac{1}{\sigma_0^2}\left(-V_0^2 \ln \frac{V}{V_0} + \frac{R_0^2 V_0^2}{R^2}\left(1 - \frac{V_0^2}{V^2}\right) + \frac{U^2}{2}\right)} e^{-\frac{2}{R_\sigma}\left(R - R_0 + \frac{(V - V_0)R}{V_0}\right)} \frac{dU dV}{\sigma_0^2} \quad (5.19)$$

### 5.1.3 Power-law rotation curve

Instead of the flat rotation curve we now assume a rotation curve  $V_c(R) = V_0(R/R_0)^\alpha$ , with an arbitrary power index  $\alpha$ . The flat rotation curve corresponds to  $\alpha = 0$ . Then the effective potential for the radial motion of a star is

$$V_{eff} = \frac{V_0^2}{2\alpha} \left(\frac{R}{R_g^2}\right)^{2\alpha} + \frac{V_0^2 R_g^2}{2} \left(\frac{1}{R^2} - \frac{1}{R_g^2}\right) \quad (5.20)$$

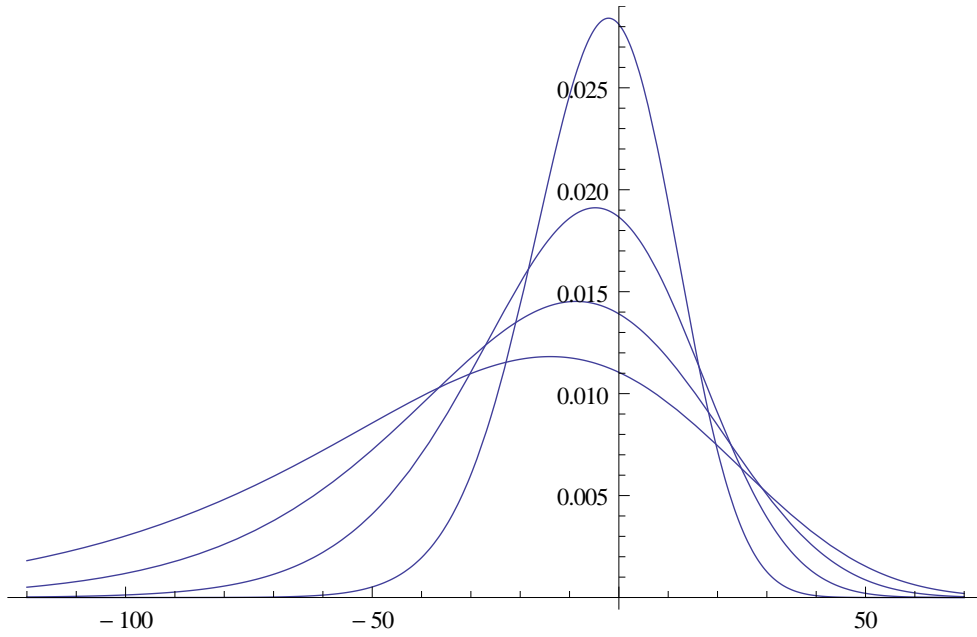


Figure 5.5: Theoretical distribution over velocities  $V$  for flat rotation curve.  $R_{\Sigma} = 2.3$  kpc,  $R_{\sigma} = 8$  kpc,  $V_0 = 240$  km/s,  $R_0 = 8$  kpc,  $\sigma_0 = 38$  km/s.

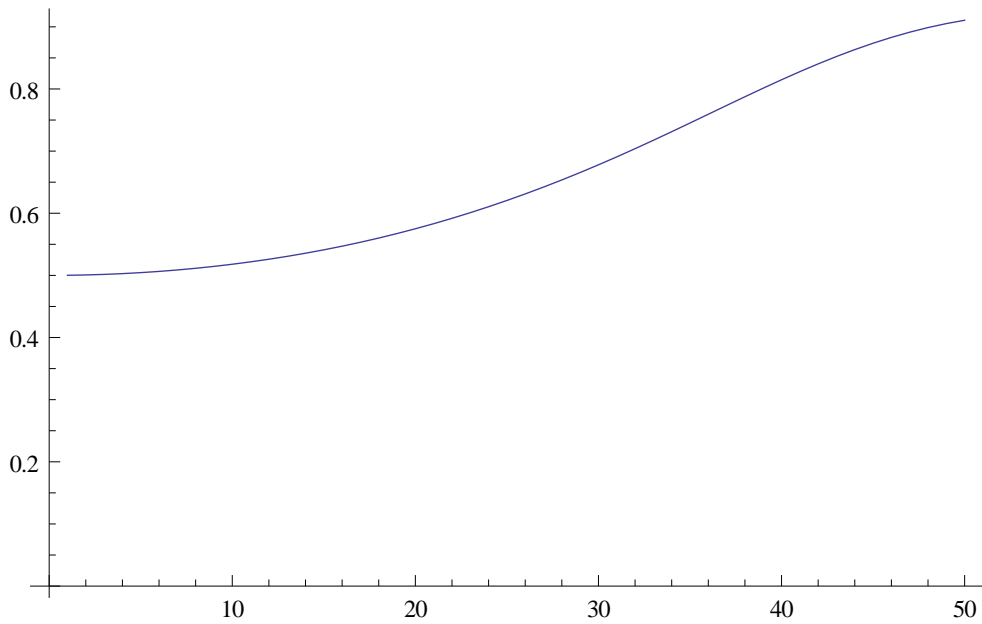


Figure 5.6: Theoretical ratio of rotational and radial velocity dispersions for flat rotation curve.  $R_{\Sigma} = 2.3$  kpc,  $R_{\sigma} = 8$  kpc,  $V_0 = 240$  km/s,  $R_0 = 8$  kpc.

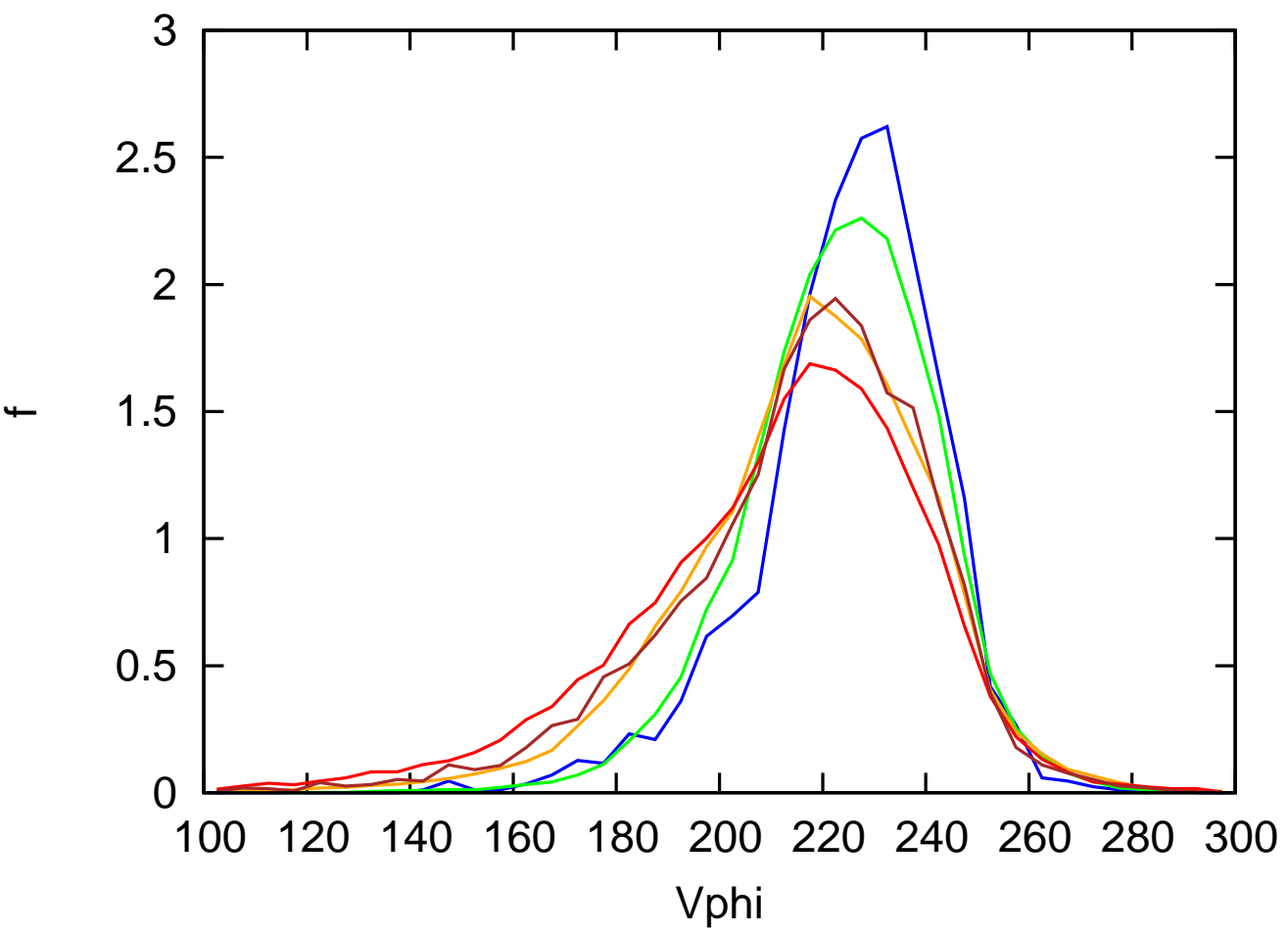


Figure 5.7: Observed distribution over velocities  $V$  from the RAVE data for 5 different colour bins.

## 5.2 Dynamical heating of the disc as a diffusion process

A distribution function  $f(I, t)$  of a 1-dimensional stellar population evolves with time according to the diffusion equation,

$$\frac{\partial f}{\partial t} = \frac{\partial}{\partial I} \left( D(I) \frac{\partial f}{\partial I} \right), \quad (5.21)$$

where  $D(I)$  is diffusion coefficient, which is assumed to be time-independent.

Let's consider a simple and important case of diffusion coefficient being proportional to a power of the action variable,  $D = D_0 I^\beta$ . The factor  $D_0$  can be easily incorporated into the time variable, thus leading us to the equation

$$\frac{\partial f}{\partial t} = \frac{\partial}{\partial I} \left( I^\beta \frac{\partial f}{\partial I} \right). \quad (5.22)$$

Let's find its self-similar solution, which is in each instant of time proportional to  $F(It^\alpha)$ , where  $\alpha$  is some constant and  $F$  is some function, which are to be determined. As  $\int f(I, t) dI$  must be independent of  $t$ , such self-similar solution can only have the form  $f = t^\alpha f(It^\alpha)$ . We substitute this solution into Eq. 5.22, and require all  $I$  and  $t$  participate in the equation only in the same combination  $x = It^\alpha$  in which they participate as the argument of  $F$ . Thus we define the power index,  $\alpha = \frac{1}{\beta-2}$ , and get for  $F$  the equation

$$(\beta - 2)x^\beta F''(x) + \beta(\beta - 2)x^{\beta-1} F'(x) - xF'(x) - F = 0 \quad (5.23)$$

In two cases the equation can be solved analytically:

- If  $\beta = 0$  then  $F(x) = e^{-\frac{x^2}{4}}$
- If  $\beta = 1$  then  $F(x) = e^{-x}$ . Only in this case we have a simple exponential distribution over energies.

For other amounts of  $\beta$  we solve Eq. 5.23 numerically and present the resulting functions in Fig. 5.8. We normalise all the solutions in such a way to have  $F(0) = 1$ . For small  $\beta$  the function  $F$  has a strong core, and then rapidly decays for  $x > 1$ , tending to the step-function when  $\beta$  tends to  $-\infty$ . For big  $\beta$  the function  $F$  is cuspy at  $x = 0$  and possesses a strong tail at big  $x$ .

Thus, the self-similar solution looks like  $f(I, t) = \frac{Const}{t^{\frac{1}{2-\beta}}} F\left(\frac{I}{t^{\frac{1}{2-\beta}}}\right)$ . For any  $\beta < 2$  it gives a distribution function, which tends to  $\delta$ -function when  $t \rightarrow 0$ , and then expands to the higher values of the angle variable, so that  $\langle I \rangle \propto t^{\frac{1}{2-\beta}}$ . For small amounts of action  $I$ , when the action  $I$  is nearly proportional to the energy  $E$ , our results imply, that a coeval population will stay isothermal only if the heating law is  $E \propto t$ . If the heating is described by a power law with a different power index, then isothermal population is inconsistent with it. For example, if we assume the heating law  $\langle E \rangle \propto t^{\frac{2}{3}}$  (as it is done in Just & Jahreiß (2010)), then  $\beta = 0.5$ , and the distribution over energies is given by the blue curve in Fig. 5.8, which is essentially more cored and has a weaker tail, than the exponential.

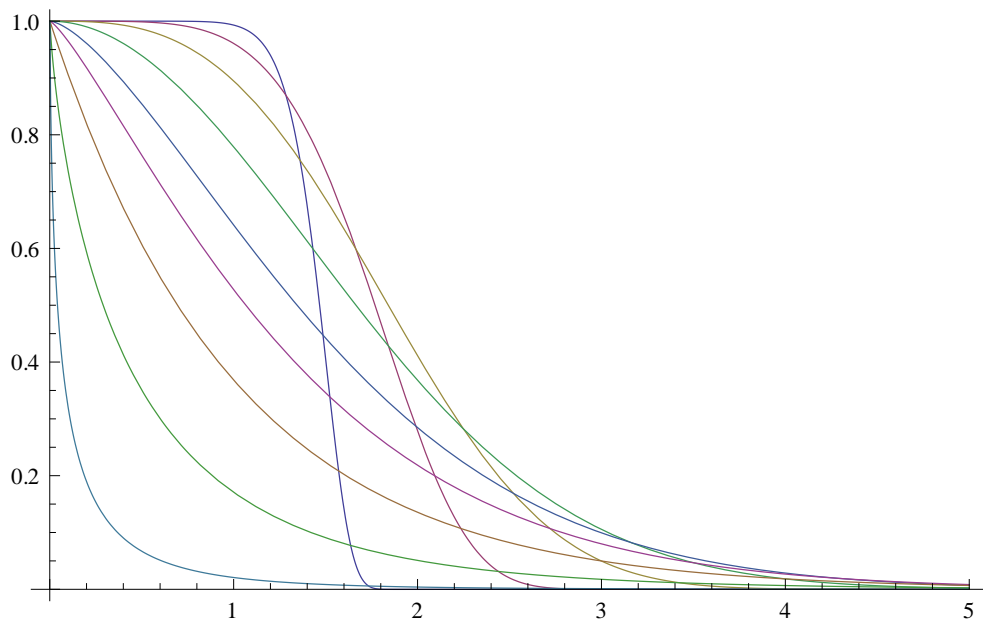


Figure 5.8: Shapes of the function  $F(x)$  for different amounts of  $\beta$ : -10 (the curve, which is the highest at  $x=1$ ), -3, -1, 0, 0.5, 0.75, 1, 1.25, 1.5 (the highest at  $x=1$ ).

## 5.3 Statistical methods for adjusting theoretical distribution functions to observational data

We discuss a variational method for constraining distribution functions with the aid of observational data. The method intrinsically accounts for observational biases and measurement errors.

### 5.3.1 General idea

Let's consider the following problem. On the one hand, we have a catalogue of observational data, which contains  $N$  stars and provides their coordinates  $\mathbf{r}_i$  and velocities  $\mathbf{v}_i$ ,  $i = 1$  to  $N$ . On the other hand, we have a family of theoretical distribution functions  $f(\mathbf{q}; \mathbf{a})$ , where  $\mathbf{q}$  is a multidimensional vector in the system's phase space, that includes all the variables on which the distribution function should depend (spatial coordinates  $\mathbf{r}$ , velocity  $\mathbf{v}$ , if available, also metallicity, age etc.), and  $\mathbf{a} = (a_1, \dots, a_M)$  is a multidimensional vector composed of free parameters of the theoretical model. The aim is to select free parameters  $\mathbf{a}$  in such a way to provide the best consistency between the theory and the observations.

A common approach to this problem is binning the data in coordinates and/or velocities, comparing number of stars in each bin with the predictions of the theoretical model, and adjusting free parameters according to  $\chi^2$  criterion. Usually this approach leads to problems connected with small-number statistics. An even more severe problem is the loss of information during binning, which augments degeneracies and sometimes even requires using several different kinds of binning to resolve them.

Here we consider a different approach. We sum logarithms of theoretical distribution function over the catalogue, thus constructing a function

$$F(\mathbf{a}) = \sum_{n=1}^N \ln f(\mathbf{q}_n; \mathbf{a}). \quad (5.24)$$

Then we adjust free parameters  $\mathbf{a}$  to maximize the function  $F$ .

Thus performed fitting is the best in the following sense. Let us consider a very big catalogue. When the number of stars  $N$  tends to infinity,  $F$  turns into

$$F = N \int d\mathbf{q} f_0(\mathbf{q}) \ln f(\mathbf{q}), \quad (5.25)$$

with  $f_0$  being the true distribution function. Let us also not constrain ourselves to the  $M$ -parametric family of functions  $f(\mathbf{r}, \mathbf{v}; \mathbf{a})$ , but search for the maximum of  $F$  throughout all possible functions  $f(\mathbf{r}, \mathbf{v})$ . Then the variational problem reads: we must optimize the functional Eq. 5.25, under the normalization constraint for the distribution function,

$$\int d\mathbf{q} f(\mathbf{q}) = 1. \quad (5.26)$$

Then the method of Lagrange multipliers leads to the equation

$$\int d\mathbf{q} \left( \frac{f_0(\mathbf{q})}{f(\mathbf{q})} - C \right) \delta f(\mathbf{q}) = 0. \quad (5.27)$$

Accounting for normalization, its solution is  $f = f_0$ , thus the theoretical distribution function that optimizes  $F$  coincides with the true distribution function.

As well we can expect, that best fitting function  $f$  will be still close to  $f_0$ , if it was searched not among all possible functions, but only among a reasonable properly chosen  $M$ -parametric set, and if the number of stars in the catalog, though not tending to infinity, is big enough.

### 5.3.2 Treating observational errors

Let us now consider the case when positions of stars in the phase space  $\mathbf{q}$  are known not precisely, but with some errors. Let  $p(\delta\mathbf{q})$  be the probability density of a star with actual phase space coordinates  $\mathbf{q}$  to be observed at the point  $\mathbf{q} + \delta\mathbf{q}$ . For the time being the probability distribution  $p(\delta\mathbf{q})$  is assumed to be the same for all stars. The normalization condition for the error distribution reads

$$\int d\delta\mathbf{q} p(\delta\mathbf{q}) = 1. \quad (5.28)$$

Now we can construct and maximize the following function

$$F(\mathbf{a}) = \sum_{n=1}^N \ln \left( \int d\delta\mathbf{q} p(\delta\mathbf{q}) f(\mathbf{q}_n - \delta\mathbf{q}; \mathbf{a}) \right). \quad (5.29)$$

For a big number of stars, the sum turns into an integral,

$$F = N \int d\mathbf{q} \int d\delta\mathbf{q}' p(\delta\mathbf{q}') f_0(\mathbf{q}) \ln \left( \int d\delta\mathbf{q} p(\delta\mathbf{q}) f(\mathbf{q} + \delta\mathbf{q}' - \delta\mathbf{q}) \right). \quad (5.30)$$

A simple transformation of variables gives

$$F = N \int d\mathbf{q} \left( \int d\delta\mathbf{q} p(\delta\mathbf{q}) f_0(\mathbf{q} - \delta\mathbf{q}) \right) \ln \left( \int d\delta\mathbf{q} p(\delta\mathbf{q}) f(\mathbf{q} - \delta\mathbf{q}) \right). \quad (5.31)$$

This expression for  $F$  is now very similar to Eq. 5.25. Moreover, Eqs. 5.26 and 5.28 provide a normalization condition,

$$\int d\mathbf{q} \int d\delta\mathbf{q} p(\delta\mathbf{q}) f(\mathbf{q} - \delta\mathbf{q}) = 1. \quad (5.32)$$

Equations 5.31 and 5.32 present a variational problem equivalent to the one presented by Eqs. 5.25 and 5.26. Method of Lagrange multipliers again results in the solution of the problem, which reads

$$\int d\delta\mathbf{q} p(\delta\mathbf{q}) f(\mathbf{q} - \delta\mathbf{q}) = \int d\delta\mathbf{q} p(\delta\mathbf{q}) f_0(\mathbf{q} - \delta\mathbf{q}). \quad (5.33)$$

It implies that  $f(\mathbf{q}) = f_0(\mathbf{q})$  is a solution of the problem. In most practical cases it is the unique solution. For example, for Gaussian errors the blurring of a distribution can be thought as a diffusion proces with some diffusion coefficients, then uniqueness of the solution follows from uniqueness of solution of a time-reversed diffusion equation.

Let us now consider the case when the errors are different for different stars,  $p = p(\delta\mathbf{q}; \Delta\mathbf{q})$ , with  $\Delta\mathbf{q}$  being parameters, describing the distribution of errors. The vector  $\Delta\mathbf{q}$  doesn't necessarily have the same number of components as  $\mathbf{q}$ . If  $\mathbf{q}$  has  $M$  components, then Gaussian errors require  $M(M + 1)/2$  components in  $\Delta\mathbf{q}$  to specify them, and non-Gaussian errors can require even more. Further, let  $P(\mathbf{q}, \Delta\mathbf{q})d\Delta\mathbf{q}$  be the probability for a star with coordinates  $\mathbf{q}$  to have the error within the range  $\Delta\mathbf{q}$  around the value  $\Delta\mathbf{q}$ . We again maximize a function similar to Eq. 5.29,

$$F(\mathbf{a}) = \sum_{n=1}^N \ln \left( \int d\delta\mathbf{q} p(\delta\mathbf{q}, \Delta\mathbf{q}_n) f(\mathbf{q}_n - \delta\mathbf{q}; \mathbf{a}) \right). \quad (5.34)$$

For a big number of stars Eq. 5.34 transforms into

$$F(\mathbf{a}) = N \int d\mathbf{q} \int d\Delta\mathbf{q} P(\mathbf{q}, \Delta\mathbf{q}) \left( \int d\delta\mathbf{q} p(\delta\mathbf{q}, \Delta\mathbf{q}) f_0(\mathbf{q} - \delta\mathbf{q}) \right) \ln \left( \int d\delta\mathbf{q} p(\delta\mathbf{q}, \Delta\mathbf{q}) f(\mathbf{q} - \delta\mathbf{q}) \right). \quad (5.35)$$

This expression must be maximized with the normalization condition,

$$\int d\mathbf{q} \int d\Delta\mathbf{q} P(\mathbf{q}, \Delta\mathbf{q}) \int d\delta\mathbf{q} p(\delta\mathbf{q}, \Delta\mathbf{q}) f_0(\mathbf{q} - \delta\mathbf{q}). \quad (5.36)$$

This problem also leads to the equation

$$\int d\delta\mathbf{q} p(\delta\mathbf{q}, \Delta\mathbf{q}) f(\mathbf{q} - \delta\mathbf{q}) = \int d\delta\mathbf{q} p(\delta\mathbf{q}, \Delta\mathbf{q}) f_0(\mathbf{q} - \delta\mathbf{q}). \quad (5.37)$$

This also implies, that  $f(\mathbf{q}) = f_0(\mathbf{q})$  is a solution. For small Gaussian errors the solution must also be unique. But sophisticated error distributions allowing multiple solutions can also be constructed.

If some components of  $\mathbf{q}$  are not measured at all (for example, a catalogue without radial velocities), we still can use the data, but must set the error for the lacking components to be infinite.

### 5.3.3 Biased samples

If a sample is biased with a known bias function  $b(\mathbf{q})$  (which is the probability for a star with a given position, velocity, mass, age etc. to be observed), then Eq. 5.24 must be transformed into

$$F(\mathbf{a}) = \frac{1}{N} \sum_{n=1}^N \frac{\ln f(\mathbf{q}_n; \mathbf{a})}{b(\mathbf{q}_n)}. \quad (5.38)$$

In the limit of a big number of stars Eq. 5.42 transforms into the same formula Eq. 5.25, and thus also leads to the correct distribution function as the best fitting value.

If the survey is magnitude- or distance-limited, we expect to observe essentially no stars in some regions of phase space. If occasionally some outliers happen to be observed in these regions, they contribute to the function Eq. 5.42 too strongly due to a very small denominator. This problem can be solved by prescribing any weighting function  $w(\mathbf{q})$  and considering variational problem

$$F(\mathbf{a}) = \frac{1}{N} \sum_{n=1}^N \frac{w(\mathbf{q}_n) \ln f(\mathbf{q}_n; \mathbf{a})}{b(\mathbf{q}_n)}, \quad (5.39)$$

$$\int d\mathbf{q} w(\mathbf{q}) f(\mathbf{q}) = 1. \quad (5.40)$$

In particular,  $w$  can be set to be equal 0 in the region we want to exclude out of the consideration at all.

Another important case is a sample with an unknown bias. Let's assume that the sample is unbiased in a subspace of phase space coordinates  $\mathbf{q}_v$ , while in the other coordinates  $\mathbf{q}_r$  is biased in an unknown manner. (The direct sum of subsets  $\mathbf{q}_v$  and  $\mathbf{q}_r$  equals to the entire phase space  $\mathbf{q}$ .) A typical example of this sort of bias is a sample with no velocity biases, but strong biases in coordinates. In this case  $\mathbf{q}_v = \mathbf{v}$ , while  $\mathbf{q}_r$  includes coordinates  $\mathbf{r}$  and some additional variables, like absolute magnitude and colour.

In this case we can still adjust the distribution function by a similar method. Instead of  $f$ , we introduce a new function

$$g(\mathbf{q}_v, \mathbf{q}_r; \mathbf{a}) = \frac{f(\mathbf{q}_v, \mathbf{q}_r; \mathbf{a})}{\int d\mathbf{q}_v f(\mathbf{q}_v, \mathbf{q}_r; \mathbf{a})}. \quad (5.41)$$

We use  $g$  to construct a function

$$F(\mathbf{a}) = \sum_{n=1}^N \ln g(\mathbf{q}_{v_n}, \mathbf{q}_{r_n}; \mathbf{a}). \quad (5.42)$$

Then we maximize this function  $F(\mathbf{a})$  with the constraint, which follows from the definition Eq. 5.41,

$$\int d\mathbf{q}_v g(\mathbf{q}_v, \mathbf{q}_r) = 1. \quad (5.43)$$

In the limit of a big number of points  $F$  is proportional to

$$F = N \int d\mathbf{q} b(\mathbf{q}_r) f_0(\mathbf{q}_v, \mathbf{q}_r) \ln g(\mathbf{q}_v, \mathbf{q}_r). \quad (5.44)$$

Here  $b(\mathbf{q}_r)$  is again the bias function, the probability for a star to be observed. It is assumed to depend on the variables from the subset  $\mathbf{q}_r$  only. Solving the variational problem of maximizing Eq. 5.44 under constraint Eq. 5.43 with the aid of Lagrange multipliers brings us to the equation

$$\int d\mathbf{q}_v d\mathbf{q}_r \left( \frac{b(\mathbf{q}_r) f_0(\mathbf{q}_v, \mathbf{q}_r)}{g(\mathbf{q}_v, \mathbf{q}_r)} - C(\mathbf{q}_v) \right) \delta f(\mathbf{q}_v, \mathbf{q}_r) = 0, \quad (5.45)$$

with  $C$  being an arbitrary function depending on  $\mathbf{q}_v$  only. Thus we get Euler's equation

$$g(\mathbf{q}_v, \mathbf{q}_r) = \frac{b(\mathbf{q}_r)f_0(\mathbf{q}_v, \mathbf{q}_r)}{C(\mathbf{q}_r)}. \quad (5.46)$$

We substitute the result into Eq. 5.41, and get

$$f(\mathbf{q}_v, \mathbf{q}_r) = C'(\mathbf{q}_r)f_0(\mathbf{q}_v, \mathbf{q}_r), \quad (5.47)$$

where  $C'(\mathbf{q}_r) = b(\mathbf{q}_r) \int d\mathbf{q}_v f(\mathbf{q}_v, \mathbf{q}_r)/C(\mathbf{q}_r)$  is an unknown function that depends on  $\mathbf{q}_v$  only. Thus  $f = f_0$  is a solution of the variational equation, though it's by far not unique when searching among all possible functions.

But constraining ourselves to the range of physically reasonable functions  $f(\mathbf{q}_v, \mathbf{q}_r; \mathbf{a})$  instead of all possible functions  $f(\mathbf{q}_v, \mathbf{q}_r)$  helps us to remove the degeneracy, as functions  $f(\mathbf{q}_v, \mathbf{q}_r; \mathbf{a})$  for different amounts of  $\mathbf{a}$  can't usually be obtained from one another by multiplying by a factor  $C'(\mathbf{q}_r)$  depending only on a part of variables. For example, two distribution functions can't have the same velocity distribution in every locus of space, but different density distributions, as it will fall into contradiction with Jeans equations, thus any factor depending on spatial coordinates can be eliminated for a velocity unbiased sample. On the other hand, an unknown factor depending on colours and magnitudes can't be eliminated without more sophisticated assumptions, like IMF and SFR.

### 5.3.4 Error estimate

When maximizing  $F$  from Eq. 5.24 we are expectin to get

$$\langle F \rangle = N \langle \ln f(\mathbf{q}) \rangle = N \int d\mathbf{q} f(\mathbf{q}) \ln f(\mathbf{q}) \quad (5.48)$$

$$\Delta F^2 = \langle (F - \langle F \rangle)^2 \rangle = N \int d\mathbf{q} f(\mathbf{q}) (\ln f(\mathbf{q}) - \langle \ln f(\mathbf{q}) \rangle)^2 \quad (5.49)$$

If if the amount of  $F$  for the best-fitting function falls within the interval  $\langle F \rangle \pm \Delta F^2$ , then the fitting can be considered to be successful. The resulting  $F$  significantly exceeding  $\langle F \rangle + \Delta F^2$  implies an unsuccessful fitting and either a wrong family of theoretical distribution functions, an unaccounted bias, or another mistake.

Let's assume that everything was right, and for  $\mathbf{a} = 0$  the distribution function really turns into the true distribution function,  $f(\mathbf{q}; \mathbf{0}) = f_0(\mathbf{q})$ . Let's estimate the error in the best fitting amount of  $\mathbf{a}$  due to the shot noise. By differentiating Eq. 5.24 we get the system of equation

$$\sum_{n=1}^N \frac{1}{f(\mathbf{q}_n; \mathbf{a})} \frac{\partial f(\mathbf{q}_n; \mathbf{a})}{\partial a_i} = 0 \quad (5.50)$$

There are  $M$  such equations for  $i = 1, \dots, M$ , with  $M$  being the number of variables. Now we expand Eqs. 5.50 into Taylor's series, obtaining

$$\sum_{j=1}^M \sum_{n=1}^N \frac{f_{ij}f - f_i f_j}{f^2} = \sum_{n=1}^N \frac{f_i}{f} \quad (5.51)$$

Here we use shorthand notation  $f_i = \partial f(\mathbf{q}_n; \mathbf{a}) / \partial a_i |_{\mathbf{a}=\mathbf{0}}$ . Summation over  $n$  means substitution  $\mathbf{q}_n$  as arguments into all functions. Now we multiply  $M$  equalities Eq. 5.51 by each other, and average the resulting products. Thus we get

$$\sum_{j,l=1}^M \left( \int \frac{f_{ij}f - f_i f_j}{f} dq \right) \left( \int \frac{f_{kl}f - f_k f_l}{f} dq \right) \langle a_j a_l \rangle = \frac{\delta_{ik}}{N} \int \frac{f_i^2}{f^2} dq \quad (5.52)$$

These  $M(M+1)$  independent equations allow us to compute the variance matrix  $\langle a_j a_l \rangle$ . Though these equations can be too complex for practical purposes if  $M$  is big, their qualitative result is still obvious: errors  $\Delta a_i$  are proportional to  $N^{-1/2}$ , and can be estimated as

$$\Delta a_i \sim \frac{a_{0i}}{N^{1/2}}, \quad (5.53)$$

where  $a_{0i}$  is the minimal change of  $a_i$  necessary to substantially change  $f$ . A similar system Eq. 5.52 can be written for  $F$  being defined by Eq. 5.29. In this case the distribution function blurred by errors must be substituted into Eq. 5.52 instead of the original one. As such blurring normally softens the gradients, and the derivatives participate in the left hand side of Eq. 5.52 in higher powers than in the right hand side, as a rule of thumb we can expect that this will increase the errors in  $a_i$ .

### 5.3.5 Applications

If we have several different stellar samples and are applying different methods of the ones described above, we can add up fitness functions  $F$  of different methods and maximize the sum. As the true distribution function must maximize all the fitness functions separately, it must also maximize their sum. But adding them together can make the error of the fitting smaller, and even resolve some degeneracies produced by different sorts of biases and errors in different catalogues.



# 6

## Summary

RAVE, SEGUE and Hipparcos data were used to study the dynamics of stars in the extended solar neighbourhood. The asymmetric drift of thin disc dwarfs as a function of velocity dispersion was found to depend on metallicity. This dependence is consistent with the known radial metallicity distribution in the disc and with our understanding of inside-out Galaxy formation. Linear extrapolation of the data give the LSR within the error bars from the one by Aumer & Binney (2009).

Implying the asymmetric drift correction to the SEGUE data allows us to reconstruct the behaviour of the rotation curve of the Milky Way in the extended solar neighbourhood. The rotation curve appears to be essentially flat, giving no hint for a dip just outside the solar radius followed by an increase observed in some other data sets. The data are supplemented by tangent point measurements for the inner rotation curve and by estimates of the gravitational potential of the outer Galaxy from the dynamics of open clusters and satellite galaxies.

We construct a 3-component density model of the Milky Way as a sum of Dehnen bulge, an exponential disc with a hole, and a flattened dark matter halo with either cored isothermal or NFW profile. We adjust the free parameters in such a way, to get the best fit of the observational data Sofue et al. (2009) and a flat rotation curve in the solar neighbourhood. When adjusting the parameters we constrain ourselves with the local surface density of the disc  $\Sigma_{\text{disc}} = 45.2 \pm 4 M_{\odot}/pc^2$  and the local volume density of the dark matter halo  $\rho_{h,0} = 0.014 M_{\odot}/pc^3$  Just & Jahreiß (2010).

Thus we get a 3-component density model of the Milky Way. The density of the bulge is given by Dehnen model with power index  $\gamma = 0.5$ , total mass  $M_b = 1.8 \times 10^{10} M_{\odot}$ , and the scale radius of  $a_b = 0.22$  kpc., The disc is exponential with  $R_d = 2.5$  kpc with a hole of a twice smaller scalelength with  $\epsilon = 0.4$ . Two different models of dark matter halo are considered, spherical cored isothermal halo with core radius  $a = 3.2$  kpc, and flattened NFW profile with  $a = 20$  kpc. Both models succeed to reproduce the data, with a somewhat better fitness for the one with cored isothermal profile.

Vertical structure of the disc of the Milky Way was studied using predominantly the RAVE sample. The results were found to be consistent with the model by Just & Jahreiß (2010), which had been constructed using the Hipparcos sample. We also reconstructed distribution of stars over energies of vertical motion.



# Bibliography

- Anderson, E. & Francis, C. 2012, *Astronomy Letters*, 38, 331
- Aumer, M. & Binney, J. J. 2009, *MNRAS*, 397, 1286
- Bienaymé, O. 1999, *A&A*, 341, 86
- Binney, J. 2010, *MNRAS*, 401, 2318
- Binney, J. & Tremaine, S. 2008, *Galactic Dynamics: Second Edition* (Princeton University Press)
- Boeche, C., Siebert, A., Williams, M., et al. 2011, *AJ*, 142, 193
- Bovy, J., Rix, H.-W., Hogg, D. W., et al. 2012, *ApJ*, 755, 115
- Breddels, M. A., Smith, M. C., Helmi, A., et al. 2010, *A&A*, 511, A90
- Coşkunoğlu, B., Ak, S., Bilir, S., et al. 2012, *MNRAS*, 419, 2844
- Coşkunoğlu, B., Ak, S., Bilir, S., et al. 2011, *MNRAS*, 412, 1237
- Dehnen, W. 1993, *MNRAS*, 265, 250
- Dehnen, W. 1999, *ApJL*, 524, L35
- Dehnen, W. & Binney, J. J. 1998, *MNRAS*, 298, 387
- Demers, S. & Battinelli, P. 2007, *A&A*, 473, 143
- Fich, M., Blitz, L., & Stark, A. A. 1989, *ApJ*, 342, 272
- Flynn, C. & Fuchs, B. 1994, *MNRAS*, 270, 471
- Frinchaboy, P. M. & Majewski, S. R. 2008, *AJ*, 136, 118
- Gillessen, S., Eisenhauer, F., Fritz, T. K., et al. 2009, *ApJL*, 707, L114
- Golubov, O. & Just, A. 2012, submitted to *MNRAS*
- Golubov, O., Just, A., Beers, T. C., & Lee, Y. S. 2012, in *European Physical Journal Web of Conferences*, Vol. 19, *European Physical Journal Web of Conferences*, 1006
- Gonzalez, O. A., Rejkuba, M., Minniti, D., et al. 2011, *A&A*, 534, L14
- Holmberg, J. & Flynn, C. 2004, *MNRAS*, 352, 440
- Holmberg, J., Nordström, B., & Andersen, J. 2009, *A&A*, 501, 941
- Honma, M., Bushimata, T., Choi, Y. K., et al. 2007, , 59, 889

- Honma, M. & Sofue, Y. 1997a, , 49, 539
- Honma, M. & Sofue, Y. 1997b, , 49, 453
- Just, A., Gao, S., & Vidrih, S. 2011, MNRAS, 411, 2586
- Just, A. & Jahreiß, H. 2010, MNRAS, 402, 461
- Kuijken, K. & Gilmore, G. 1991, ApJL, 367, L9
- Lee, Y. S., Beers, T. C., An, D., et al. 2011, ApJ, 738, 187
- Maciel, W. J. & Lago, L. G. 2005, , 41, 383
- McMillan, P. J. 2011, MNRAS, 414, 2446
- Nakashima, J.-i., Jiang, B. W., Deguchi, S., Sadakane, K., & Nakada, Y. 2000, , 52, 275
- Navarro, J. F., Frenk, C. S., & White, S. D. M. 1996, ApJ, 462, 563
- Nishiyama, S., Nagata, T., Baba, D., et al. 2005, ApJL, 621, L105
- Nordström, B., Mayor, M., Andersen, J., et al. 2004, A&A, 418, 989
- Oh, C. S., Kobayashi, H., Honma, M., et al. 2010, , 62, 101
- Reid, M. J. 1993, ARA&A, 31, 345
- Reid, M. J. & Brunthaler, A. 2005, in *Astronomical Society of the Pacific Conference Series*, Vol. 340, *Future Directions in High Resolution Astronomy*, ed. J. Romney & M. Reid, 253
- Reid, M. J., Menten, K. M., Zheng, X. W., et al. 2009, ApJ, 700, 137
- Robin, A. C., Reylé, C., Derrière, S., & Picaud, S. 2003, A&A, 409, 523
- Scannapieco, C., Wadeuphl, M., Parry, O. H., et al. 2012, MNRAS, 423, 1726
- Schönrich, R., Binney, J., & Dehnen, W. 2010, MNRAS, 403, 1829
- Siebert, A., Famaey, B., Binney, J., et al. 2012, in preparation
- Siebert, A., Williams, M. E. K., Siviero, A., et al. 2011, AJ, 141, 187
- Sofue, Y., Honma, M., & Omodaka, T. 2009, , 61, 227
- Springel, V., White, S. D. M., Jenkins, A., et al. 2005, Nature, 435, 629
- Turon, C., Primas, F., Binney, J., et al. 2008, The Messenger, 134, 46
- West, A. A., Morgan, D. P., Bochanski, J. J., et al. 2011, AJ, 141, 97
- Zwitter, T., Matijević, G., Breddels, M. A., et al. 2010, A&A, 522, A54

# Acknowledgements

I acknowledge funding by IMPRS for Astronomy & Cosmic Physics at the University of Heidelberg.

Funding for RAVE has been provided by: the Australian Astronomical Observatory; the Leibniz-Institut für Astrophysik Potsdam (AIP); the Australian National University; the Australian Research Council; the French National Research Agency; the German Research Foundation (SPP 1177 and SFB 881); the European Research Council (ERC-StG 240271 Galactica); the Istituto Nazionale di Astrofisica at Padova; The Johns Hopkins University; the National Science Foundation of the USA (AST-0908326); the W. M. Keck foundation; the Macquarie University; the Netherlands Research School for Astronomy; the Natural Sciences and Engineering Research Council of Canada; the Slovenian Research Agency; the Swiss National Science Foundation; the Science & Technology Facilities Council of the UK; Opticon; Strasbourg Observatory; and the Universities of Groningen, Heidelberg and Sydney. The RAVE web site is at <http://www.rave-survey.org>.

Funding for SDSS-I and SDSS-II has been provided by the Alfred P. Sloan Foundation, the Participating Institutions, the National Science Foundation, the U.S. Department of Energy, the National Aeronautics and Space Administration, the Japanese Monbukagakusho, the Max Planck Society, and the Higher Education Funding Council for England. The SDSS Web Site is <http://www.sdss.org/>.

My scientific advisor Andreas Just supported me very much both scientifically and psychologically, and without his help this thesis could never be written. I received many good advices from my thesis committee members Eva Grebel and Glenn van de Ven. I am very grateful to Young-Sun Lee and Timothy C. Beers for providing their SEGUE data sample for our analysis and for fruitful discussions, and to Hartmuth Jahreiß for providing me with results of his analysis of the local stellar samples; to my friends and officemates Xiaoying Pang, Jan Rybizki, Mohamad Abbas; to my other friends, to my teachers, and to my family.

Heidelberg  
Oleksiy Golubov  
September 24, 2012

